Journal of Fluids and Structures 102 (2021) 103246

Contents lists available at ScienceDirect

Journal of Fluids and Structures

journal homepage: www.elsevier.com/locate/jfs

A BEM model for wave forces on structures with thin porous elements

Ed Mackay [a,*], Hui Liang [b], Lars Johanning [a]

[a] College of Engineering, Mathematics and Physical Sciences, University of Exeter, TR10 9FE, UK
[b] Technology Centre for Offshore and Marine, Singapore (TCOMS), 118411, Singapore

ARTICLE INFO

Article history:
Received 20 August 2020
Received in revised form 3 December 2020
Accepted 5 February 2021
Available online xxxx

Keywords:
Porous
Slotted
Perforated
Boundary element method

ABSTRACT

A boundary element method (BEM) model is presented for wave forces on structures composed of solid and porous surfaces, where the porous surface can be subject to either a linear or quadratic pressure–velocity relation. In the case of the quadratic relation, the solutions to the radiation and diffraction problems cannot be superimposed to obtain a solution for body motions in waves. Instead, a solution method is proposed which solves for the motion response and wave forces on the body simultaneously. Solutions for the radiation and diffraction problems are then obtained as special cases. Hydrodynamic identities and expressions for the mean drift force for combined solid-porous bodies are also derived. It is shown that in the case of a quadratic pressure drop, the hydrodynamic coefficients are no longer symmetric and the Haskind relation must be modified to account for the pressure drop across the porous surface. The BEM solution is verified against an analytical calculations and results for the excitation and mean drift forces are shown to agree well. A case study is presented for a floating truncated cylinder, with a concentric porous outer cylinder. It is shown that the porous outer cylinder significantly increases the damping at low frequencies, where wave radiation damping is low, leading to a lower motion response.

1. Introduction

The problem of calculating wave forces on structures with perforated or porous elements arises in a range of engineering contexts. Fixed and floating breakwaters often contain chambers with slatted or perforated fronts, designed to dissipate wave energy (Huang et al., 2011; Dai et al., 2018). Porous plates or meshes are sometimes used for absorbing waves in narrow flumes (Twu and Lin, 1991; Molin and Fourest, 1992), motion damping of marine structures (Williams et al., 2000; Lee and Ker, 2002; Molin, 2011; Vijay and Sahoo, 2018) or cages used for aquaculture (Zhao et al., 2010a; Dokken et al., 2017a). Porous plates are also used to dissipate energy in tuned liquid dampers (Tait et al., 2005; Faltinsen et al., 2011; Crowley and Porter, 2012; Molin and Remy, 2013, 2015).

There is a wide literature on modelling wave interaction with porous structures. Computational fluid dynamics (CFD) approaches (e.g. Valizadeh et al., 2018; Chen et al., 2019; Mentzoni and Kristiansen, 2019; Poguluri and Cho, 2020) offer a flexible solution for modelling the complex features of the flow through the porous surface for arbitrary body geometries. In these approaches, the flow through the openings in the porous surfaces is modelled explicitly. This requires a numerical mesh which resolves both the small-scale features of the openings in the porous surface and the large-scales required for wave propagation, resulting in high numbers of mesh cells and correspondingly high computational times.

* Corresponding author.
E-mail address: e.mackay@exeter.ac.uk (E. Mackay).

https://doi.org/10.1016/j.jfluidstructs.2021.103246

Alternatively, potential flow methods based on linear wave theory are often used. In these approaches, the flow through the openings in the porous surface is not modelled explicitly, but is parameterised in terms of a pressure drop as a function of flow velocity, with either a linear or quadratic pressure–velocity relation. It is possible to derive analytical models for the wave interaction with simple structures such as vertical barriers (Chwang, 1983; Chwang and Li, 1983; Yu, 1995; Isaacson et al., 1998; Sahoo et al., 2000) or cylinders (Wang and Ren, 1994; Williams et al., 2000; Zhao et al., 2010b; Ning et al., 2017; Cong and Liu, 2020). For more complex structures, numerical approaches such as the boundary element method (BEM) are required. BEM models for wave interactions with porous structures in two dimensions have been applied widely (Ijima et al., 1976; Sulisz, 1985; Mallayachari and Sundar, 1994; Yueh and Tsaur, 1999; Chen et al., 2004; Cho and Kim, 2008; Liu et al., 2012; Gayen and Mondal, 2014; Yueh et al., 2016; Liu and Li, 2017; Mackay et al., 2019; Vijay et al., 2019, 2020; Mackay and Johanning, 2020). More recently, BEM models for wave interaction with fully porous bodies (i.e. with no solid elements) in three dimensions have been developed (Dokken et al., 2017a,b; Ouled Housseine et al., 2018). BEM models for solid bodies with dissipative surfaces have recently been developed (Feng et al., 2018; Lee and Zhu, 2018). In these models, the dissipative surfaces are subject to a pressure drop similar to that used for porous surfaces. The models proposed in Feng et al. (2018), Lee and Zhu (2018) use a hyper-singular integral equation method to solve for the flow across a surface subject to a linear pressure–velocity relation. A multi-domain BEM approach for solid bodies with porous elements was presented in Mackay et al. (2018), for the case where the porous surface is subject to a linear pressure–velocity relation.

The purpose of the present study is to extend the approaches presented in Dokken et al. (2017a,b), Mackay et al. (2018) and present a 3D BEM model for wave interaction with solid structures containing porous elements, subject to either linear or quadratic pressure–velocity relations. In the current approach, we assume that the porous surface encloses a bounded region, where one of the boundaries can be the free surface.

The focus here is on the case with the quadratic pressure drop across the porous surface, with the linear case included for comparison and verification. In the case of a linear pressure drop, the solutions of the radiation and diffraction problems can be superimposed in the usual way to obtain the motion response of the structure. In the case of the quadratic pressure drop, this superposition is no longer valid due to the nonlinear pressure–velocity relations on the porous surface. Instead, we propose a solution method which solves for the motion response and wave forces on the body simultaneously. Solutions for the radiation and diffraction problems are then obtained as special cases.

In this paper, we present a verification of the BEM solution against an analytical model for bottom-fixed vertical cylinder with a concentric porous outer cylinder subject to a linear pressure drop (Wang and Ren, 1994; Cong and Liu, 2020). We also present a case study of a floating truncated cylinder, with a concentric porous outer cylinder subject to a quadratic pressure drop. It is shown that the porous outer cylinder can significantly reduce the motion response of the structure. The validation of the methodology against physical experiments is presented in a separate paper (Mackay et al., 2020).

Zhao et al. (2011) derived hydrodynamic identities and expressions for the mean drift force, for the case of fully-porous bodies subject to a linear pressure drop. In this work we extend some of these relations to the case of a combined solid-porous body subject to either a linear or quadratic pressure drop. It is shown that in the case of a quadratic pressure drop, the hydrodynamic coefficients are no longer symmetric and the Haskind relation must be modified to account for the pressure drop across the porous surface. Although the BEM solution proposed here assumes that the porous surface encloses a bounded region, the hydrodynamic identities derived and expressions for the mean drift force also apply to the case where the porous surface does not enclose a bounded region (e.g. a porous plate).

The paper is organised as follows. The mathematical formulation of the problem is presented in Section 2 and the BEM solution is presented in Section 3. Hydrodynamic identities for structures with both solid and porous elements are derived in Section 4 and an expression for the mean drift force is derived in Section 5. The verification of the BEM solution against results from an analytical model is presented in Section 6. A case study is presented in Section 7, for the wave loads and motion response of a floating truncated cylinder with a porous outer wall. Finally, conclusions are presented in Section 8.

2. Problem formulation

The structure is assumed to consist of a single solid body and a porous surface bounding a volume of water connected to this body. The geometry of the solid body and porous surface are arbitrary and may be either submerged or surface-piercing. The surface of the solid body is divided into two parts, an exterior solid surface, S_E, and an interior solid surface, S_I. The porous surface is denoted S_P. The fluid domain is divided into regions external and internal to the porous boundary, denoted D^E and D^I. A sketch of the setup and notation is shown in Fig. 1, which shows a truncated cylinder with a solid inner column and porous outer surface.

The normal vectors on S_E are defined to point out of D^E and the normal vectors on S_P and S_I are defined to point into D^I (see Fig. 1). This convention is adopted so that all normal vectors point out of D^E and into D^I. The coordinate system is defined with $z = 0$ on the free surface and $z = -h$ on the sea bed, where h can be either finite or infinite. The porosity of S_P is denoted τ and defined as the ratio of the area of the openings to the total area of porous surface.

The thickness of the porous barrier and the spacing of the openings are both assumed to be small relative to the incident wavelength, so that the barrier can be treated as a homogeneous surface with a pressure jump across it. The flow through the openings is not modelled explicitly, but approximated using a model for the dissipative and inertial

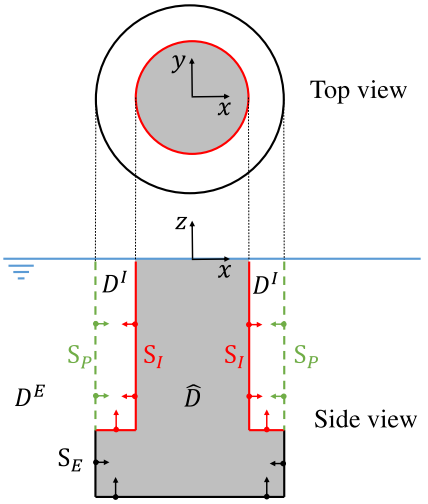

Fig. 1. Sketch of definition of surfaces, normal vectors and internal and external fluid domains.

effects as a function of the fluid velocity and acceleration. The effects of the barrier thickness and spacing of the openings are assumed to be captured by the model for the pressure drop across the porous barrier.

The flow through the porous surface is subject to both viscous drag and turbulent dissipation of energy. However, it is assumed that the wakes are quickly homogenised into the flow within a short distance of the porous surface. Away from the porous surface, the fluid is assumed to be inviscid and incompressible, and its motion irrotational, so that a velocity potential can be used to describe the fluid motion. The potentials in the exterior and interior domains denoted Φ^E and Φ^I.

2.1. Decomposition of potentials

The structure is subject to regular linear waves of amplitude A and angular frequency ω, propagating in a direction at an angle β to the positive x-axis (i.e. $\beta = 0$ corresponds to waves propagating from negative to positive x). The structure is assumed to make 6-DOF harmonic motions of amplitude ξ_j, $j = 1, \ldots, 6$, corresponding to surge, sway, heave, roll, pitch and yaw. Under these assumptions the potentials in each domain can be written as

$$\Phi(\mathbf{x}, t)^{E,I} = \mathrm{Re}\left\{ e^{i\omega t} \frac{igA}{\omega} \phi^{E,I}(\mathbf{x}) \right\}, \tag{1}$$

where g is the acceleration due to gravity, $\mathbf{x} = (x, y, z)$ is the position vector and $\phi^{E,I}(\mathbf{x})$ is the non-dimensional complex amplitude of the potential in each domain. The spatial component is decomposed as

$$\phi^{E,I} = \phi_0 + \phi_7^{E,I} + \sum_{j=1}^{6} \frac{\xi_j}{A} \phi_j^{E,I}, \tag{2}$$

where ϕ_0 is the incident wave potential, $\phi_7^{E,I}$ is the diffracted wave potential and $\phi_j^{E,I}$, $j = 1, \ldots, 6$, are the radiated potentials for each mode of motion. Note that ϕ_j is non-dimensional for $j = 1, 2, 3$, but has the dimension of length for $j = 4, 5, 6$. However, the same formulation is used for consistency of notation. The normalisations in (1) and (2) have been used so that the boundary conditions on the porous surface take the same form for both the radiation and diffraction problems (see Section 2.3). In the case of forced motion without incident waves we set $A = \xi_j$ and $\phi_0 = \phi_7 = 0$.

The scattered wave potential is defined as the sum of the diffracted and radiated potentials:

$$\phi_s^{E,I} = \phi_7^{E,I} + \sum_{j=1}^{6} \frac{\xi_j}{A} \phi_j^{E,I}. \tag{3}$$

The potentials in each domain satisfy the Laplace equation, the linearised free-surface condition and the no-flow condition on the seabed:

$$\nabla^2 \phi_j^{E,I} = 0, \qquad j = 0, \ldots, 7, \tag{4}$$

$$\frac{\partial \phi_j^{E,I}}{\partial z} = K \phi_j^{E,I}, \qquad z = 0, \quad j = 0, \ldots, 7, \tag{5}$$

$$\frac{\partial \phi_j^{E,I}}{\partial z} = 0, \qquad z = -h, \quad j = 0, \ldots, 7, \tag{6}$$

where $K = \omega^2/g$ is the infinite-depth wavenumber.

The incident wave potential is given by

$$\phi_0 = Z(kz)\exp(-ik(x\cos\beta + y\sin\beta)), \tag{7}$$

where β is the wave direction, k is the finite-depth wavenumber, defined as the positive real solution of $K = k\tanh(kh)$ and the function $Z(kz)$ is defined as

$$Z(kz) = \begin{cases} \frac{\cosh(k(z+h))}{\cosh(kh)} & \text{in finite depth,} \\ \exp(kz) & \text{in infinite depth.} \end{cases} \tag{8}$$

The radiated and diffracted potentials in the exterior domain satisfy a radiation condition in the far-field

$$\lim_{R\to\infty} \sqrt{R}\left(\frac{\partial \phi_j^E}{\partial R} + ik\phi_j^E\right) = 0, \quad j = 1, \ldots, 7, \tag{9}$$

where $R = \sqrt{x^2 + y^2}$.

2.2. Boundary conditions on solid surfaces

The normal vector to the body surface is denoted $\mathbf{n} = (n_1, n_2, n_3)$ and the additional notation $(n_4, n_5, n_6) = \mathbf{x} \times \mathbf{n}$ is adopted. Using this notation, the normal velocity of the boundary of the structure is given by

$$U_n = \mathrm{Re}\left\{e^{i\omega t} i\omega \sum_{j=1}^{6} \xi_j n_j\right\} = \mathrm{Re}\left\{e^{i\omega t} i\omega A u_n\right\}, \tag{10}$$

where u_n is a non-dimensionalised velocity of the body surface, defined by

$$u_n = \sum_{j=1}^{6} \frac{\xi_j}{A} n_j. \tag{11}$$

The boundary condition for the scattered potential on the solid surfaces can therefore be written as

$$\frac{1}{K}\frac{\partial \phi_s^{E,I}}{\partial n} = n_s, \quad \text{on} \quad S_E, S_I, \tag{12}$$

where n_s is defined as

$$n_s = n_7 + u_n \tag{13}$$

and

$$n_7 = -\frac{1}{K}\frac{\partial \phi_0}{\partial n}. \tag{14}$$

For fixed structures or for forced motion of a structure in still water, the diffraction and radiation problems can be solved in isolation. In these cases, the boundary conditions for the diffraction and radiation potentials on the solid surfaces are

$$\frac{1}{K}\frac{\partial \phi_j^{E,I}}{\partial n} = n_j, \quad \text{on} \quad S_E, S_I, \quad j = 1, \ldots, 7. \tag{15}$$

2.3. Boundary conditions on porous surfaces

The flow through the porous surface in the normal direction is assumed to be continuous on either side of the boundary, so the kinematic boundary condition on the porous surfaces is

$$\frac{\partial \phi_s^E}{\partial n} = \frac{\partial \phi_s^I}{\partial n}, \quad \text{on} \quad S_P. \tag{16}$$

The pressure drop, ΔP, across the porous boundary is assumed to be the sum of three terms, a linear drag term related to the viscosity of the fluid, a quadratic drag term due to flow separation and an inertial term due to acceleration of the flow through the openings (Sollitt and Cross, 1972):

$$\frac{\Delta P}{\rho} = \frac{\nu}{l} W_n + \frac{1}{2} C_f W_n |W_n| + L\frac{\partial W_n}{\partial t}, \tag{17}$$

where ρ is the fluid density, W_n is the fluid velocity relative to the porous boundary in the normal direction (assumed to be the average velocity close to the porous boundary rather than the flow speed through the openings), ν is the kinematic viscosity of the fluid, l is a coefficient with the dimension of length, C_f is a dimensionless drag coefficient and L is an inertial coefficient with the dimension of length. The fluid velocity through the porous boundary is the difference between the fluid velocity and boundary velocity, given by

$$W_n = V_n - U_n = \mathrm{Re}\left\{e^{i\omega t} i\omega A w_n\right\}, \tag{18}$$

where V_n is the velocity of the fluid in the direction normal to the body surface. V_n can be written as

$$V_n = \frac{\partial \Phi}{\partial n} = \mathrm{Re}\left\{e^{i\omega t} i\omega A v_n\right\}, \tag{19}$$

where v_n is the non-dimensional amplitude of the velocity of the fluid given by

$$v_n = \frac{1}{K}\frac{\partial \phi}{\partial n}. \tag{20}$$

We can therefore write

$$w_n = v_n - u_n. \tag{21}$$

The dynamic pressure is given by the linearised Bernoulli equation as

$$P = -\rho \frac{\partial \Phi}{\partial t} = \rho g A \mathrm{Re}\left\{\phi e^{i\omega t}\right\}. \tag{22}$$

Different boundary conditions on the porous surfaces can be derived depending on whether it is assumed that the linear or quadratic drag term in (17) is dominant. The two cases will be treated in turn below. Note that if it is assumed that both quadratic drag and inertial effects can be ignored then (17) reduces to Darcy's law.

2.3.1. Formulation for linear pressure drop

If it is assumed that the quadratic terms in (17) can be neglected, then substituting (18) and (22) into (17) and factoring out the time dependence gives the relation

$$w_n = -i\sigma_l \left(\phi^E - \phi^I\right), \tag{23}$$

where σ_l is a non-dimensional linear porosity coefficient given by

$$\sigma_l = \frac{1}{K(f + iL)}, \tag{24}$$

where $f = \nu/\omega l$ is a resistance coefficient with dimension of length. The linear boundary condition is more commonly specified in terms of the 'porous effect parameter', G (Chwang, 1983; Chwang and Li, 1983). In the current notation, the porous effect parameter is defined by the relation

$$K\sigma_l = kG = \frac{1}{f + iL}. \tag{25}$$

In some studies, where the porous boundary is assumed to have finite thickness, δ, the porous effect parameter is defined as $kG = \tau/\delta(\gamma + is)$, where γ and s are dimensionless friction and inertial coefficients (Yu, 1995). Empirical models for γ and s have been derived by various authors (e.g. Li et al., 2006; Suh et al., 2011; Liu and Li, 2016). In the present work, we assume that the porous boundary has negligible thickness, and G is defined by (25), with f and L both having units of length.

2.3.2. Formulation for quadratic pressure drop

In the quadratic formulation, it is assumed that the linear drag term in (17) can be neglected. The time dependence in the quadratic term in (17) can be linearised using Lorenz's principle of equivalent work:

$$W_n |W_n| \approx \frac{8}{3\pi}(\omega A)^2 |w_n| \,\mathrm{Re}\left\{e^{i\omega t} i w_n\right\}. \tag{26}$$

Substituting (22) and (26) into (17) gives

$$w_n = -i\sigma_q \left(\phi^E - \phi^I\right), \tag{27}$$

where σ_q is a non-dimensional quadratic porosity coefficient given by

$$\sigma_q = \left(\frac{4}{3\pi} C_f K A |w_n| + iKL\right)^{-1}. \tag{28}$$

Note that σ_q is dependent on both the wave amplitude and the dimensionless velocity w_n, whereas σ_l is not. The coefficients C_f and L could, in principle, be modelled as a function of flow velocity using the iterative framework described

in Section 3. However, in the present work C_f and L are assumed to be known constants. Models for C_f and L are reviewed in Molin (2011), Huang et al. (2011), Mackay and Johanning (2020). In the case study presented in Section 7, we use Molin and Fourest's model (Molin and Fourest, 1992) for C_f, given by

$$C_f = \frac{1-\tau}{\mu\tau^2}, \tag{29}$$

where μ is an empirically defined discharge coefficient, set at 0.5 for the present work.

2.3.3. Dynamic boundary conditions on porous surfaces

Eqs. (23) and (27) can be used to define dynamic boundary conditions on the porous surface for the scattered potential in the combined radiation–diffraction case, the diffraction potential in the fixed case or the radiation potential for the forced motion case. For the scattered potential we have

$$\frac{1}{K}\frac{\partial\phi_s}{\partial n} = n_s - i\sigma\left(\phi_s^E - \phi_s^I\right), \quad \text{on} \quad S_P, \tag{30}$$

where σ is either σ_l or σ_q, depending on whether the linear or quadratic formulations are used. In the radiation problem, the same formulation can be used if we assume ξ_j is real and set $A = \xi_j$ and $\phi_0 = \phi_7 = 0$. For both the diffraction and radiation potentials the dynamic boundary condition on the porous surface is

$$\frac{1}{K}\frac{\partial\phi_j}{\partial n} = n_j - i\sigma\left(\phi_j^E - \phi_j^I\right), \quad \text{on} \quad S_P, \quad j = 1,\ldots,7. \tag{31}$$

2.4. Linear forces and moments

Once the potential is known, the total hydrodynamic force (or moment) on the structure in the jth mode, $F_{H,j}$, is the sum of the force (or moment) on the internal and external surfaces

$$F_{H,j} = \rho g A\left[\int_{S_E\cup S_P}\phi^E n_j \mathrm{d}S - \int_{S_I\cup S_P}\phi^I n_j \mathrm{d}S\right], \quad j = 1,\ldots,6. \tag{32}$$

Note that the surface normal vectors are pointing in the opposite direction in the interior domain so the integral over the interior surfaces has the opposite sign. Similarly, for the diffraction problem, the excitation force (or moment) in the jth mode, F_j, is given by

$$F_j = \rho g A\left[\int_{S_E\cup S_P}\left(\phi_0^E + \phi_7^E\right) n_j \mathrm{d}S - \int_{S_I\cup S_P}\left(\phi_0^I + \phi_7^I\right) n_j \mathrm{d}S\right], \quad j = 1,\ldots,6. \tag{33}$$

For the radiation problem, the added mass, a_{ij}, and damping coefficients, b_{ij}, are defined by

$$\omega^2 a_{ij} - i\omega b_{ij} = \rho g\left[\int_{S_E\cup S_P}\phi_j^E n_i \mathrm{d}S - \int_{S_I\cup S_P}\phi_j^I n_i \mathrm{d}S\right]. \tag{34}$$

The damping of the motion is due to wave radiation and drag through the porous elements. The separation of the damping coefficient into components due to radiation and dissipation is discussed in Section 4.2. The mean drift force on the body will be considered in Section 5.

3. BEM solution

In this section we consider a BEM solution for the general case of the scatter potential, ϕ_s, for a floating body subject to incident waves. The radiation and diffraction problems are special cases of the general solution. The formulation is applicable to both the linear and quadratic pressure drop cases. However, in the case of the quadratic formulation, the radiation and diffraction problems cannot be superimposed to derive the general solution for body motions in waves, due to the nonlinear pressure drop across the porous surface. Instead, we solve for the combined solution simultaneously.

Application of Green's third identity to the domain bounded by the external body surfaces (S_E and S_P), the free surface, the sea bed and a control surface at infinity yields the following integral equation for the scattered potential in the exterior domain (see e.g. Linton and Mciver (2001):

$$\int_{S_E\cup S_P}\left(\phi_s^E(\boldsymbol{\xi})\frac{\partial\mathcal{G}(\mathbf{x},\boldsymbol{\xi})}{\partial n_{\boldsymbol{\xi}}} - \frac{\partial\phi_s^E(\boldsymbol{\xi})}{\partial n_{\boldsymbol{\xi}}}\mathcal{G}(\mathbf{x},\boldsymbol{\xi})\right)\mathrm{d}S = \begin{cases} -4\pi\phi_s^E(\mathbf{x}), & \mathbf{x}\in D_E, \\ -2\pi\phi_s^E(\mathbf{x}), & \mathbf{x}\in S_E\cup S_P, \\ 0, & \mathbf{x}\in\hat{D}, \end{cases} \tag{35}$$

where $\boldsymbol{\xi}$ is the source point on the body surface, and $\mathbf{x}$ is the field point, either on the body external surface, in the external domain, D_E, or in the domain inside the body $\hat{D}$. The extension of the integral equations to $\hat{D}$ is required for the suppression of the effects of irregular frequencies, as described in Section 3.3. $\mathcal{G}$ is the free surface Green function, defined below, which satisfies boundary conditions (4)–(6) and (9). Note that the integrals over the free surface, sea bed

and control surface vanish as a result of the conditions (5), (6) and (9). Similarly, application of Green's third identity to the interior domain yields the following integral equation for the scattered potential in the interior domain:

$$\int_{S_I \cup S_P} \left(\phi_s^I(\boldsymbol{\xi}) \frac{\partial \mathcal{G}(\mathbf{x}, \boldsymbol{\xi})}{\partial n_{\boldsymbol{\xi}}} - \frac{\partial \phi_s^I(\boldsymbol{\xi})}{\partial n_{\boldsymbol{\xi}}} \mathcal{G}(\mathbf{x}, \boldsymbol{\xi}) \right) \mathrm{d}S = \begin{cases} 4\pi \phi_s^I(\mathbf{x}), & \mathbf{x} \in D_I, \\ 2\pi \phi_s^I(\mathbf{x}), & \mathbf{x} \in S_I \cup S_P, \\ 0, & \mathbf{x} \in \hat{D}, . \end{cases} \tag{36}$$

Note that the opposite sign occurs on the RHS as the surface normal vectors are pointing into the fluid in the interior domain.

The Green function describes the linearised potential at point $\mathbf{x} = (x, y, z)$ due to a pulsating source at point $\boldsymbol{\xi} = (\xi, \eta, \zeta)$. In infinite depth, the Green function can be written as (John, 1950)

$$\mathcal{G} = \frac{1}{r_1} + \frac{1}{r_2} + 2K \int_0^\infty \frac{e^{\nu(z+\zeta)}}{\nu - K} J_0(\nu r_0) \mathrm{d}\nu \tag{37}$$

and in finite depth it can be written as

$$\mathcal{G} = \frac{1}{r_1} + \frac{1}{r_3} + \int_0^\infty \frac{2(\nu + K)\cosh(\nu(z+h))\cosh(\nu(\zeta+h))}{\nu \sinh(kh) - K\cosh(kh)} e^{-\nu h} J_0(\nu r_0) \mathrm{d}\nu, \tag{38}$$

where J_0 is the zero order Bessel function of the first kind and

$$r_0 = \left((x-\xi)^2 + (y-\eta)^2\right)^{1/2}, \tag{39}$$

$$r_1 = \left(r_0 + (z-\zeta)^2\right)^{1/2}, \tag{40}$$

$$r_2 = \left(r_0 + (z+\zeta)^2\right)^{1/2}, \tag{41}$$

$$r_3 = \left(r_0 + (z+\zeta+2h)^2\right)^{1/2}. \tag{42}$$

The integrals in (37) and (38) are evaluated using contour integration, with the contour indented above the pole on the real axis to satisfy the radiation condition. For the infinite depth case, the Green function is computed using the method described by Chen (1993). In finite depth, the Green function is computed using the method described by Mackay (2019).

The integral Eqs. (35) and (36) are solved by discretising the body surface into a number of flat panels, with N_E panels on S_E, N_I panels on S_I and N_P panels on S_P. The panels on the porous surface are used for both the interior and exterior boundary integrals. The points $\mathbf{x}_i = (x_i, y_i, z_i)$, where the integral equations are enforced, are defined to be at the panel centroids. The panels are numbered with those on solid parts coming first, followed by the panels on the porous parts of the structure, so that $\boldsymbol{\phi}_s^{ES} = \left[\phi_s^E(\mathbf{x}_1), \ldots, \phi_s^E(\mathbf{x}_{N_E})\right]^T \boldsymbol{\phi}$ are the scattered potentials at the centroids of the solid panels of the exterior surface and $\boldsymbol{\phi}_s^{EP} = \left[\phi_s^E(\mathbf{x}_{N_E+1}), \ldots, \phi_s^E(\mathbf{x}_{N_E+N_P})\right]^T \boldsymbol{\phi}$ are the scattered potentials at the centroids of the exterior porous panels. Similarly, define $\boldsymbol{\phi}_s^{IS} = \left[\phi_s^I(\mathbf{x}_1), \ldots, \phi_s^I(\mathbf{x}_{N_I})\right]^T \boldsymbol{\phi}$ and $\boldsymbol{\phi}_s^{IP} = \left[\phi_s^I(\mathbf{x}_{N_I+1}), \ldots, \phi_s^I(\mathbf{x}_{N_I+N_P})\right]^T \boldsymbol{\phi}$ to be the scattered potentials on the solid and porous panels of interior surface.

Define coefficient matrices for the interior and exterior problems, $\mathbf{D}^E$, $\mathbf{D}^I$, $\mathbf{S}^E$, $\mathbf{S}^I$, as

$$D_{ij}^E = 2\pi\delta_{ij} + \int_{S_j} \frac{\partial \mathcal{G}(\mathbf{x}_i, \mathbf{x}_j)}{\partial n_j} \mathrm{d}S, \tag{43}$$

$$D_{ij}^I = -2\pi\delta_{ij} + \int_{S_j} \frac{\partial \mathcal{G}(\mathbf{x}_i, \mathbf{x}_j)}{\partial n_j} \mathrm{d}S, \tag{44}$$

$$S_{ij}^{E,I} = \int_{S_j} \mathcal{G}(\mathbf{x}_i, \mathbf{x}_j) \mathrm{d}S, \tag{45}$$

where S_j is the surface of the jth panel (of the exterior/interior problem respectively) and δ_{ij} is the Kronecker delta function. For now we assume that $\mathbf{x}_i$ is on one of the body surfaces, so that D^E, D^I, S^E and S^I are square matrices. The integrals of the Rankine terms in the Green function and its derivative are computed using the algorithms in Newman (1986) and the remaining parts are assumed to be constant over each panel. The coefficient matrices can be written as block matrices

$$\mathbf{D}^{E,I} = \begin{bmatrix} \mathbf{D}_{SS}^{E,I} & \mathbf{D}_{SP}^{E,I} \\ \mathbf{D}_{PS}^{E,I} & \mathbf{D}_{PP}^{E,I} \end{bmatrix}, \quad \mathbf{S}^{E,I} = \begin{bmatrix} \mathbf{S}_{SS}^{E,I} & \mathbf{S}_{SP}^{E,I} \\ \mathbf{S}_{PS}^{E,I} & \mathbf{S}_{PP}^{E,I} \end{bmatrix}, \tag{46}$$

where the submatrices $\mathbf{D}_{SS}^{E,I}$, $\mathbf{S}_{SS}^{E,I}$ and $\mathbf{D}_{PP}^{E,I}$, $\mathbf{S}_{PP}^{E,I}$ correspond to the terms between the solid and porous panels respectively and the other submatrices correspond to the remaining terms. If it is assumed that the potential is constant on each panel, then the integral Eqs. (35) and (36) can then be written in discrete form:

$$\begin{bmatrix} \mathbf{D}_{SS}^E & \mathbf{D}_{SP}^E \\ \mathbf{D}_{PS}^E & \mathbf{D}_{PP}^E \end{bmatrix} \begin{bmatrix} \boldsymbol{\phi}_s^{ES} \\ \boldsymbol{\phi}_s^{EP} \end{bmatrix} = K \begin{bmatrix} \mathbf{S}_{SS}^E & \mathbf{S}_{SP}^E \\ \mathbf{S}_{PS}^E & \mathbf{S}_{PP}^E \end{bmatrix} \begin{bmatrix} \mathbf{n}_7^{ES} + \mathbf{u}_n^{ES} \\ \mathbf{n}_7^{EP} + \mathbf{u}_n^{EP} - i\boldsymbol{\sigma} \circ \left(\boldsymbol{\phi}_s^{EP} - \boldsymbol{\phi}_s^{IP}\right) \end{bmatrix}, \tag{47}$$

$$\begin{bmatrix} \mathbf{D}_{SS}^{I} & \mathbf{D}_{SP}^{I} \\ \mathbf{D}_{PS}^{I} & \mathbf{D}_{PP}^{I} \end{bmatrix} \begin{bmatrix} \boldsymbol{\phi}_s^{IS} \\ \boldsymbol{\phi}_s^{IP} \end{bmatrix} = K \begin{bmatrix} \mathbf{S}_{SS}^{I} & \mathbf{S}_{SP}^{I} \\ \mathbf{S}_{PS}^{I} & \mathbf{S}_{PP}^{I} \end{bmatrix} \begin{bmatrix} \mathbf{n}_7^{IS} + \mathbf{u}_n^{IS} \\ \mathbf{n}_7^{IP} + \mathbf{u}_n^{IP} - i\boldsymbol{\sigma} \circ \left(\boldsymbol{\phi}_s^{EP} - \boldsymbol{\phi}_s^{IP} \right) \end{bmatrix}, \tag{48}$$

where the superscripts denote the values on the panels of the solid/porous parts of the exterior/interior surfaces respectively. In the expressions above, the boundary condition (12) has been applied on the solid panels and (30) has been applied on the porous panels. The vector $\boldsymbol{\sigma}$ represents the values on each panel of either σ_l or σ_q, depending on whether a linear or quadratic pressure drop is assumed. In the linear case, σ_l is constant over all panels, whereas in the quadratic case, σ_q varies over each panel, depending on the value of w_n. The notation $\mathbf{x} \circ \mathbf{y}$ denotes the Hadamard product (i.e. elementwise multiplication).

Combining these two systems of equations gives a single matrix equation for the potentials in the interior and exterior domains:

$$\begin{bmatrix} \mathbf{D}_{SS}^{E} & \mathbf{D}_{SP}^{E} + iK\boldsymbol{\sigma} \circ \mathbf{S}_{SP}^{E} & \mathbf{0} & -iK\boldsymbol{\sigma} \circ \mathbf{S}_{SP}^{E} \\ \mathbf{D}_{PS}^{E} & \mathbf{D}_{PP}^{E} + iK\boldsymbol{\sigma} \circ \mathbf{S}_{PP}^{E} & \mathbf{0} & -iK\boldsymbol{\sigma} \circ \mathbf{S}_{PP}^{E} \\ \mathbf{0} & iK\boldsymbol{\sigma} \circ \mathbf{S}_{SP}^{I} & \mathbf{D}_{SS}^{I} & \mathbf{D}_{SP}^{I} - iK\boldsymbol{\sigma} \circ \mathbf{S}_{SP}^{I} \\ \mathbf{0} & iK\boldsymbol{\sigma} \circ \mathbf{S}_{PP}^{I} & \mathbf{D}_{PS}^{I} & \mathbf{D}_{PP}^{I} - iK\boldsymbol{\sigma} \circ \mathbf{S}_{PP}^{I} \end{bmatrix} \begin{bmatrix} \boldsymbol{\phi}_s^{ES} \\ \boldsymbol{\phi}_s^{EP} \\ \boldsymbol{\phi}_s^{IS} \\ \boldsymbol{\phi}_s^{IP} \end{bmatrix} = K \begin{bmatrix} \mathbf{S}_{SS}^{E} & \mathbf{S}_{SP}^{E} & \mathbf{0} & \mathbf{0} \\ \mathbf{S}_{PS}^{E} & \mathbf{S}_{PP}^{E} & \mathbf{0} & \mathbf{0} \\ \mathbf{0} & \mathbf{0} & \mathbf{S}_{SS}^{I} & \mathbf{S}_{SP}^{I} \\ \mathbf{0} & \mathbf{0} & \mathbf{S}_{PS}^{I} & \mathbf{S}_{PP}^{I} \end{bmatrix} \begin{bmatrix} \mathbf{n}_7^{ES} + \mathbf{u}_n^{ES} \\ \mathbf{n}_7^{EP} + \mathbf{u}_n^{EP} \\ \mathbf{n}_7^{IS} + \mathbf{u}_n^{IS} \\ \mathbf{n}_7^{IP} + \mathbf{u}_n^{IP} \end{bmatrix} \tag{49}$$

In the linear pressure drop case, $\boldsymbol{\sigma}$ is known and the radiation and diffraction problems can be solved separately. However, in the quadratic pressure drop case, the system of equations above has two sets of unknowns in addition to the potential: the normalised 6DOF velocity of the structure, $\boldsymbol{u_n}$, and the normalised velocity of the fluid on the porous panels $\boldsymbol{w_n}$, which appears in the quadratic porosity coefficient, σ_q(28). The approach taken to solve the system involves two loops. In the inner loop, we iterate to find the fluid velocity, based on a first guess of the motion amplitude in each degree of freedom. In the outer loop we iterate to find the motion amplitude. An attempt was made to solve for the motion amplitude and fluid velocity in the same loop, however this proved to be unstable.

3.1. Inner loop for fluid velocity

The inner loop assumes specified motion amplitudes ξ_j and hence a fixed value of u_n. The problem is solved iteratively, with a first guess of $w_n = -n_s$, i.e. the fluid velocity due to the scattered potential is assumed to be zero. On panels where the first guess of w_n is zero, the first guess of σ_q is ∞ (this occurs when the inertial coefficient L is zero and panels are vertical and perpendicular to the incident wave direction in the diffraction case or panels are perpendicular to the body motion direction for radiation cases). To avoid numerical issues, the first guess of w_n is set to 10^{-4} in these cases. The following steps are then taken on each iteration:

1. Calculate σ_q using (28)
2. Solve the system (49) for the scattered potentials
3. Calculate the normal velocity from the scattered potential, $\partial\phi_s/\partial n$, on the porous panels using (30)
4. Define the new value of fluid normal velocity as the average of the previous estimate and the new estimate calculated in step 3.

The iterations are terminated when the maximum value of $|\phi_s^m - \phi_s^{m-1}|$ is less than 10^{-4}. Typically, around 10–15 iterations are required for convergence.

3.2. Outer loop for body velocity

In the outer loop, the body motion amplitude is found which satisfies the equation of motion, based on the hydrodynamic forces from the potential calculated in the inner loop. The radiation and diffraction problems cannot be decoupled, due to the quadratic dependence on flow velocity through the porous surface. The equation of motion must therefore be written in terms of the total hydrodynamic force as

$$\boldsymbol{F}_H - \mathcal{M}\boldsymbol{\xi} = 0, \tag{50}$$

where $\boldsymbol{F}_H$ is the total hydrodynamic force vector defined in (32) and $\boldsymbol{\xi}$ is the body motion amplitude vector. The matrix $\mathcal{M}$ is given by

$$\mathcal{M} = \mathbf{C}_m + \mathbf{C}_{HS} - \omega^2 \left(\mathbf{M}_b + \mathbf{M}_m \right) + i\omega \mathbf{B}_m, \tag{51}$$

where $\mathbf{C}_m$, $\mathbf{B}_m$ and $\mathbf{M}_m$ are the linearised mooring stiffness, damping and mass matrices and $\mathbf{M}_b$ is the body mass matrix. $\mathbf{C}_{HS}$ is the hydrostatic stiffness matrix. It is assumed that $\mathbf{C}_{HS}$ also includes the stiffness terms accounting for the change in the moment of the centre of mass about the centre of rotation, where the linearised roll moment is $mgx_g\xi_6 - mgz_g\xi_4$ and linearised pitch moment is $mgy_g\xi_6 - mgz_g\xi_5$, m is the body mass and (x_g, y_g, z_g) is the position of the centre of mass relative to the centre of rotation.

To solve the equation of motion, we write $\mathcal{F}(\boldsymbol{\xi}) = \boldsymbol{F}_H(\boldsymbol{\xi}) - \mathcal{M}\boldsymbol{\xi}$, where $\boldsymbol{F}_H(\boldsymbol{\xi})$ is the total hydrodynamic force corresponding to body motion vector $\boldsymbol{\xi}$ and the incident wave conditions, and the potential is calculated as described in the previous section. We then solve $\mathcal{F}(\boldsymbol{\xi}) = 0$ using a Levenberg–Marquardt method (see e.g. Moré (1978), based on a first guess of $\boldsymbol{\xi} = 0$. In the current work this has been implemented via the MATLAB function '*fsolve*'.

3.3. Removal of irregular frequencies

It is well known that the boundary integral equations do not have a unique solution at certain so-called "irregular frequencies". The irregular frequencies correspond to eigen solutions of the interior boundary-value problem with a Dirichlet-type condition on the interior body surface and a Robin-type condition on the interior free surface. Various methods have been proposed to define a unique solution over all frequencies. In this work, we have adopted the approach of Lau and Hearn (1989), which extends the domain of the integral equations to the interior of the body, $\hat{D}$. Assuming that the body extends through the mean free surface, we define $\hat{S}$ to be the intersection of the body and mean free surface. We add, $\hat{N}$, field points on $\hat{S}$, giving an additional set of equations to be solved. The additional equations are only used for the exterior problem. These result in an over-determined system of equations with the resultant coefficient matrices $\mathbf{D}^E$ and $\mathbf{S}^E$ being of size $(N_E + N_P + \hat{N}) \times (N_E + N_P)$. The matrices $\mathbf{D}^E$ and $\mathbf{S}^E$ are converted back to square matrices of size $(N_E + N_P) \times (N_E + N_P)$ by multiplying each side of (47) by $(\mathbf{D}^E)^T$, where the superscript T denotes the transpose. The equations for the interior and exterior problems are then combined into a single system in the same way as described above. A similar method for removing irregular frequency effects from BEM calculations of wave interactions with combined solid-porous structures was presented by Liang et al. (2020), but with the additional constraint that the horizontal components of the fluid velocity are zero on the internal free surface.

4. Hydrodynamic identities

Various hydrodynamic identities can be derived using Green's theorem and considering various pairs of potentials. This was first done systematically by Newman (1976), but as noted in that study, many of these results had been known individually for a long time. Zhao et al. (2011) followed Newman's systematic approach to derive similar results for the case of a fully porous body with a linear pressure drop. In this section we extend some of these results for bodies composed of both solid and porous surfaces, with either linear or quadratic dissipation.

We start by considering two arbitrary potentials, φ and ψ, which satisfy the free-surface and bottom boundary conditions and the boundary conditions on the solid and porous surfaces. Applying Green's theorem to the domain bounded by the exterior surface of the body, the free surface, the sea bed and a stationary control surface at infinity gives

$$\int_{S_E \cup S_P} \left(\varphi^E \frac{\partial \psi^E}{\partial n} - \psi^E \frac{\partial \varphi^E}{\partial n} \right) \mathrm{d}S = - \int_{S_\infty} \left(\varphi^E \frac{\partial \psi^E}{\partial n} - \psi^E \frac{\partial \varphi^E}{\partial n} \right) \mathrm{d}S. \tag{52}$$

Similarly, application of Green's theorem to the interior domain gives

$$\int_{S_I \cup S_P} \left(\varphi^I \frac{\partial \psi^I}{\partial n} - \psi^I \frac{\partial \varphi^I}{\partial n} \right) \mathrm{d}S = 0. \tag{53}$$

Subtracting (53) from (52) gives a relation between potentials on the body surface and the far field:

$$\int_{S_E \cup S_P} \left(\varphi^E \frac{\partial \psi^E}{\partial n} - \psi^E \frac{\partial \varphi^E}{\partial n} \right) \mathrm{d}S - \int_{S_I \cup S_P} \left(\varphi^I \frac{\partial \psi^I}{\partial n} - \psi^I \frac{\partial \varphi^I}{\partial n} \right) \mathrm{d}S = - \int_{S_\infty} \left(\varphi^E \frac{\partial \psi^E}{\partial n} - \psi^E \frac{\partial \varphi^E}{\partial n} \right) \mathrm{d}S. \tag{54}$$

4.1. Symmetry of hydrodynamic coefficients

If $\varphi = \phi_i$ and $\psi = \phi_j$ are radiation potentials, satisfying the radiation condition (9), then the integral over the control surface at infinity is zero and (52) and (53) can be combined to give

$$\int_{S_E} \left(\phi_i^E \frac{\partial \phi_j^E}{\partial n} - \phi_j^E \frac{\partial \phi_i^E}{\partial n} \right) \mathrm{d}S - \int_{S_I} \left(\phi_i^I \frac{\partial \phi_j^I}{\partial n} - \phi_j^I \frac{\partial \phi_i^I}{\partial n} \right) \mathrm{d}S = - \int_{S_P} \left((\phi_i^E - \phi_i^I) \frac{\partial \phi_j}{\partial n} - (\phi_j^E - \phi_j^I) \frac{\partial \phi_i}{\partial n} \right) \mathrm{d}S. \tag{55}$$

In the expression above the superscripts on the normal derivatives on the porous surface have been dropped due to the continuity of velocity across the porous surface. Substituting the boundary conditions on the solid and porous surfaces gives

$$\left[\int_{S_E \cup S_P} \phi_i^E n_j \mathrm{d}S - \int_{S_I \cup S_P} \phi_i^I n_j \mathrm{d}S \right] - \left[\int_{S_E \cup S_P} \phi_j^E n_i \mathrm{d}S - \int_{S_I \cup S_P} \phi_j^I n_i \mathrm{d}S \right] = \int_{S_P} i(\sigma_j - \sigma_i)(\phi_i^E - \phi_i^I)(\phi_j^E - \phi_j^I) \mathrm{d}S. \tag{56}$$

The terms σ_i and σ_j are the porosity coefficients, either linear or quadratic, corresponding to the radiation problems in modes i and j. From the definition of the added mass and damping coefficients (34) we have

$$a_{ji} - a_{ij} = \mathrm{Re} \left[\frac{\rho g}{\omega^2} \int_{S_P} i(\sigma_j - \sigma_i)(\phi_i^E - \phi_i^I)(\phi_j^E - \phi_j^I) \mathrm{d}S \right], \tag{57}$$

$$b_{ji} - b_{ij} = -\mathrm{Im} \left[\frac{\rho g}{\omega} \int_{S_P} i(\sigma_j - \sigma_i)(\phi_i^E - \phi_i^I)(\phi_j^E - \phi_j^I) \mathrm{d}S \right]. \tag{58}$$

In the case of linear dissipation, σ_l is constant over the structure and independent of the motion of the structure, so $\sigma_i = \sigma_j$ and hence $a_{ji} = a_{ij}$ and $b_{ji} = b_{ij}$. In contrast, for the case of quadratic dissipation, σ_q varies over the structure and is dependent on w_n. Therefore $\sigma_i \neq \sigma_j$ for $i \neq j$, since the velocity distribution across the body will differ for each mode of motion. So the added mass and damping matrices are no longer symmetric in the case of quadratic dissipation through the porous surface.

4.2. Wave radiation and porous damping

Zhao et al. (2011) and Dokken et al. (2017a) showed that the damping coefficient could be expressed as a sum of two terms, one due to wave radiation and the other due to dissipation through the porous surface. In both these cases, the structures considered were entirely porous and the dissipation through the porous surface was linear. The derivation for the case of a combined solid-porous structure with quadratic damping is similar to that in Zhao et al. (2011). However, due to the asymmetry of the hydrodynamic coefficients in the case of quadratic dissipation through the porous surface, we only consider the diagonal elements of the damping matrix. From (34), the damping coefficient can be expressed as

$$\begin{aligned}\frac{\omega b_{jj}}{\rho g} &= -\mathrm{Im}\left[\int_{S_E\cup S_P}\phi_j^E n_j \mathrm{d}S - \int_{S_I\cup S_P}\phi_j^I n_j \mathrm{d}S\right],\\ &= -\frac{1}{2i}\left[\int_{S_E\cup S_P}\left(\phi_j^E n_j^* - (\phi_j^E)^* n_j\right)\mathrm{d}S - \int_{S_I\cup S_P}\left(\phi_j^I n_j^* - (\phi_j^I)^* n_j\right)\mathrm{d}S\right].\end{aligned} \tag{59}$$

In the second line of the equation above we have used the fact that n_j is real and hence $n_j = n_j^*$, where the star denotes the complex conjugate. Substituting the boundary conditions on the solid and porous surfaces gives

$$\frac{\omega b_{jj}}{\rho g} = -\frac{1}{2iK}\left[\int_{S_E\cup S_P}\left(\phi_j^E\frac{\partial(\phi_j^E)^*}{\partial n} - (\phi_j^E)^*\frac{\partial\phi_j^E}{\partial n}\right)\mathrm{d}S - \int_{S_I\cup S_P}\left(\phi_j^I\frac{\partial(\phi_j^I)^*}{\partial n} - (\phi_j^I)^*\frac{\partial\phi_j^I}{\partial n}\right)\mathrm{d}S\right] + \int_{S_P}\mathrm{Re}(\sigma)\left|\phi_j^E - \phi_j^I\right|^2\mathrm{d}S. \tag{60}$$

From (52) we can replace the integral over the exterior domain with an integral over a control surface at infinity and from (53) the integral over the interior domain is zero, giving

$$\frac{\omega b_{jj}}{\rho g} = \frac{1}{2iK}\int_{S_\infty}\left(\phi_j^E\frac{\partial(\phi_j^E)^*}{\partial n} - (\phi_j^E)^*\frac{\partial\phi_j^E}{\partial n}\right)\mathrm{d}S + \int_{S_P}\mathrm{Re}(\sigma)\left|\phi_j^E - \phi_j^I\right|^2\mathrm{d}S. \tag{61}$$

The first integral in the equation above is the usual contribution of wave radiation from an oscillating body and the second integral is the contribution from dissipation of energy across the porous surface. The potential in the far-field can be expressed using (35) and the far-field form of the Green function (Mei, 1983)

$$\lim_{R\to\infty}\mathcal{G} = \frac{1}{D(kh)}\sqrt{\frac{8\pi k}{R}}Z(kz)\exp\left(-i(kR+\pi/4)\right)\phi_0^*(\boldsymbol{\xi},\theta), \tag{62}$$

where $(x, y) = (R\cos\theta, R\sin\theta)$ and the function $D(kh)$ is given by

$$D(kh) = \tanh(kh) + \frac{kh}{\cosh^2 kh}. \tag{63}$$

Note that $D(kh) = 1$ in infinite water depth. Substituting (62) into (35) gives

$$\lim_{R\to\infty}\phi_j = (2\pi kR)^{-1/2}Z(kz)\exp\left(-i(kR+\pi/4)\right)H_j(\theta), \tag{64}$$

where $H_j(\theta)$ is the Kochin function, defined as

$$H_j(\theta) = \frac{k}{D(kh)}\int_{S_E\cup S_P}\left(\frac{\partial\phi_j^E(\boldsymbol{\xi})}{\partial n} - \phi_j^E(\boldsymbol{\xi})\frac{\partial}{\partial n}\right)\phi_0^*(\boldsymbol{\xi},\theta)\mathrm{d}S, \tag{65}$$

$$= \frac{Kk}{D(kh)}\left[\int_{S_E\cup S_P}\left(n_j(\boldsymbol{\xi})\phi_0^*(\boldsymbol{\xi},\theta) + \phi_j^E(\boldsymbol{\xi})n_7^*(\boldsymbol{\xi},\theta)\right)\mathrm{d}S + \int_{S_P}w_n(\boldsymbol{\xi})\phi_0^*(\boldsymbol{\xi},\theta)\mathrm{d}S\right]. \tag{66}$$

The second equality above is obtained by substituting the boundary conditions on the solid and porous surfaces. Substituting (64) into (61) and evaluating the integral over depth gives

$$b_{jj} = b_{jj}^{rad} + b_{jj}^{por} \tag{67}$$

where

$$b_{jj}^{rad} = \rho\,\omega\,\frac{1}{4\pi}\frac{D(kh)}{K^2k}\int_0^{2\pi}\left|H_j(\theta)\right|^2\mathrm{d}\theta, \tag{68}$$

$$b_{jj}^{por} = \frac{\rho g}{\omega} \int_{S_P} \frac{\mathrm{Re}(\sigma)}{|\sigma|^2} |w_n|^2 \, \mathrm{d}S. \tag{69}$$

Eq. (69) is obtained by substituting (27) into the second integral in (61). For the two cases of linear and quadratic dissipation through the porous plate we have:

$$b_{jj}^{por} = \begin{cases} \rho \omega f \int_{S_P} |w_n|^2 \, \mathrm{d}S, & \text{linear dissipation,} \\ \rho \omega \dfrac{4}{3\pi} C_f \xi_j \int_{S_P} |w_n|^3 \, \mathrm{d}S, & \text{quadratic dissipation.} \end{cases} \tag{70}$$

In the linear case the porous damping is independent of the amplitude of motion, ξ_j, whereas in the quadratic case the damping coefficient depends on both C_f and ξ_j.

4.3. Haskind relation

Zhao et al. (2011) showed that the Haskind relation for a solid body can be extended to the case of a fully porous body with a linear pressure drop. The case of a fully porous body with a quadratic pressure drop was considered by Dokken et al. (2017b). As with the previous sections, we extend these relations to the case of a combined solid-porous body with either linear or quadratic pressure drop.

The Haskind relation is derived by substituting $\varphi = \phi_0 + \phi_7$ and $\psi = \phi_j$ ($j = 1, \ldots, 6$) into (54). The integral over S_∞ can be evaluated in the same way as for solid bodies (Newman, 1976), by substituting the far-field representation of the potential (64) and using the method of stationary phase to give the right side of (54) as

$$\mathrm{RHS} = \frac{D(kh)}{k} H_j(\beta + \pi). \tag{71}$$

Substituting the boundary conditions on the solid and porous surfaces, the left side of (54) can be re-written as

$$\begin{aligned} \mathrm{LHS} &= K \left[\int_{S_E \cup S_P} (\phi_0^E + \phi_7^E) n_j \mathrm{d}S - \int_{S_I \cup S_P} (\phi_0^I + \phi_7^I) n_j \mathrm{d}S + i \int_{S_P} (\sigma_7 - \sigma_j)(\phi_7^E - \phi_7^I)(\phi_j^E - \phi_j^I) \mathrm{d}S \right] \\ &= \frac{KF_j}{\rho g A} + iK \int_{S_P} (\sigma_7 - \sigma_j)(\phi_7^E - \phi_7^I)(\phi_j^E - \phi_j^I) \mathrm{d}S. \end{aligned} \tag{72}$$

Recombining the expressions above gives a modified Haskind relation for combined solid-porous bodies

$$\frac{D(kh)}{kK} H_j(\beta + \pi) = \frac{F_j}{\rho g A} + i \int_{S_P} (\sigma_7 - \sigma_j)(\phi_7^E - \phi_7^I)(\phi_j^E - \phi_j^I) \mathrm{d}S. \tag{73}$$

The same expression was derived by Dokken et al. (2017b) for the case of fully porous bodies. In the case of linear dissipation through the porous surface we have $\sigma_7 = \sigma_j$. In this case, substituting (73) into (68) gives the usual relation between radiation damping and excitation forces

$$b_{jj}^{rad} = \frac{\rho \omega}{4\pi} \frac{k}{D(kh)} \int_0^{2\pi} \left| \frac{F_j(\beta)}{\rho g A} \right|^2 \mathrm{d}\beta. \tag{74}$$

For quadratic dissipation, $\sigma_7 \neq \sigma_j$ and (74) must be modified to include the contribution from the integral over the porous surface in (73).

5. Mean drift force

Expressions for the mean drift force on a fully porous body with a linear pressure drop have been presented by Zhao et al. (2011) and Dokken et al. (2017a). We follow a similar approach here, for the case of a combined solid-porous structure with either a linear or quadratic pressure drop. The mean drift force is calculated from the rate of change of momentum in the fluid. The rate of change of horizontal momentum in the exterior domain can be written in terms of a surface integral over the exterior surface of the body, $S_E \cup S_P$, the free surface, S_{FS}, the sea bed, S_B, and a fixed control surface at infinity, S_∞ (Maruo, 1960; Newman, 1967)

$$\frac{d}{dt} \begin{pmatrix} \mathbf{M}_x^E \\ \mathbf{M}_y^E \end{pmatrix} = - \int_\Gamma \left[P_T \begin{pmatrix} n_x \\ n_y \end{pmatrix} + \rho \begin{pmatrix} V_x \\ V_y \end{pmatrix} (V_n - U_n) \right] \mathrm{d}S, \tag{75}$$

where $\Gamma = S_E \cup S_P \cup S_{FS} \cup S_B \cup S_\infty$, $\mathbf{M}$ is the fluid momentum, V is the fluid velocity and U is the velocity of the surface. Subscripts x and y denote the components of the variables in the two horizontal directions and the subscript n denotes the component in the direction normal to the surface. P_T is the total fluid pressure, including the hydrostatic and velocity-squared components, given by the Bernoulli equation:

$$-\frac{P_T}{\rho} = gz + \frac{\partial \Phi}{\partial t} + \frac{1}{2} |\nabla \Phi|^2. \tag{76}$$

On the free surface and sea bed $V_n = U_n$. On the free surface we also have $P_T = 0$ and on the (horizontal) sea bed we have $n_x = n_y = 0$. Therefore, the integrand of (75) is zero on the free surface and sea bed. Note also that $V_n = U_n$ on S_E and $U_n = 0$ on S_∞ so (75) can be rewritten as.

$$\frac{d}{dt}\begin{pmatrix}\mathbf{M}_x^E\\ \mathbf{M}_y^E\end{pmatrix} = -\int_{S_E\cup S_P} P_T\begin{pmatrix}n_x\\ n_y\end{pmatrix}\mathrm{d}S - \int_{S_P}\rho\begin{pmatrix}V_x\\ V_y\end{pmatrix}(V_n - U_n)\mathrm{d}S \qquad -\int_{S_\infty}\left[P_T\begin{pmatrix}n_x\\ n_y\end{pmatrix} + \rho\begin{pmatrix}V_x\\ V_y\end{pmatrix}V_n\right]\mathrm{d}S. \tag{77}$$

Similarly, the rate of change of fluid momentum in the interior domain can be written as:

$$\frac{d}{dt}\begin{pmatrix}\mathbf{M}_x^I\\ \mathbf{M}_y^I\end{pmatrix} = -\int_{S_I\cup S_P} P_T\begin{pmatrix}n_x\\ n_y\end{pmatrix}\mathrm{d}S - \int_{S_P}\rho\begin{pmatrix}V_x\\ V_y\end{pmatrix}(V_n - U_n)\mathrm{d}S. \tag{78}$$

The mean drift force, $\bar{\mathbf{F}} = (\bar{F}_x, \bar{F}_y)^T$, is the time average of the integral of the fluid pressure over the body surfaces. Since the body motions are assumed to be in steady state, the time average of the rate of change of momentum is zero. Therefore, we can write:

$$\begin{aligned}\begin{pmatrix}\bar{F}_x\\ \bar{F}_y\end{pmatrix} &= \overline{\int_{S_E\cup S_P} P_T\begin{pmatrix}n_x\\ n_y\end{pmatrix}\mathrm{d}S} - \overline{\int_{S_I\cup S_P} P_T\begin{pmatrix}n_x\\ n_y\end{pmatrix}\mathrm{d}S}\\ &= -\overline{\int_{S_\infty}\left[P_T\begin{pmatrix}n_x\\ n_y\end{pmatrix} + \rho\begin{pmatrix}V_x\\ V_y\end{pmatrix}V_n\right]\mathrm{d}S} - \overline{\int_{S_P}\rho\begin{pmatrix}V_x^E - V_x^I\\ V_y^E - V_y^I\end{pmatrix}(V_n - U_n)\mathrm{d}S}.\end{aligned} \tag{79}$$

Here, the superscripts E and I have been added to the velocity terms in the final integral in (79) to distinguish between the velocity in the internal and external domains. Note that while, the velocity normal to the porous boundary is assumed to be continuous between the external and internal domains, the components of the velocity tangential to the porous surface can differ. The term involving the integral over S_∞ in (79) is the conventional far-field representation for the drift force on a solid body and the second component is due to energy dissipation across the porous surface. We will denote these two components as $\bar{\mathbf{F}}^{far}$ and $\bar{\mathbf{F}}^{por}$.

The first component can be written as (Mei, 1983)

$$\frac{1}{\rho g A^2}\begin{pmatrix}\bar{F}_x^{far}\\ \bar{F}_y^{far}\end{pmatrix} = -\frac{D(kh)}{2K}\left[\mathrm{Im}\left\{H_s(\beta)\right\}\begin{pmatrix}\cos(\beta)\\ \sin(\beta)\end{pmatrix} + \frac{1}{4\pi}\int_0^{2\pi}|H_s(\theta)|^2\begin{pmatrix}\cos(\theta)\\ \sin(\theta)\end{pmatrix}\mathrm{d}\theta\right], \tag{80}$$

where β is the incident wave direction.

The second component can be rewritten by substituting the expressions for the fluid velocity and body surface velocity and taking the time average to give

$$\frac{1}{\rho g A^2}\begin{pmatrix}\bar{F}_x^{por}\\ \bar{F}_y^{por}\end{pmatrix} = -\frac{K}{2}\mathrm{Re}\left\{\int_{S_P} w_n^*\begin{pmatrix}v_x^E - v_x^I\\ v_y^E - v_y^I\end{pmatrix}\mathrm{d}S\right\}, \tag{81}$$

and

$$v_x^{E,I} = \frac{1}{K}\frac{\partial\phi_s^{E,I}}{\partial x}, \quad v_y^{E,I} = \frac{1}{K}\frac{\partial\phi_s^{E,I}}{\partial y}. \tag{82}$$

The tangential components of the fluid velocity on the porous surface can be computed in several ways. One method is to take the spatial derivative of the integral equations for the potential (35) and (36). This method requires special treatment of the hypersingular integral arising from the second derivative of the Green function. Alternatively, the velocity on the body surface can be calculated using the source formulation (see e.g. Lee and Newman (2005). However, it was found that when the velocities were calculated using either of these methods, the effects of irregular frequencies were still visible in the velocities when using the irregular frequency removal method described in Section 3.3. In the current work, the tangential components of the velocity on a given panel have been estimated by quadratic interpolation. This approach is similar to the high-order BEM, but is applied as a post-processing stage. Details are given in the Appendix.

6. Verification

Various verification cases for the BEM model with the linear pressure drop formulation have been published in Mackay et al. (2018). The previous verification cases considered excitation forces and added mass and damping coefficients. In this section we present an additional verification of excitation forces and mean drift forces from the BEM model for the case of a bottom-fixed vertical cylinder with a porous outer wall, for the case with a linear pressure drop across the porous surface.

Consider the case of a solid bottom-fixed vertical cylinder with circular cross section, radius a, surrounded by a concentric porous cylinder, radius b, in water depth h (see Fig. 2). The cylinder is subject to waves of amplitude A propagating towards the positive x direction. The pressure drop across the porous cylinder is assumed to be linearly proportional to the fluid velocity, with porous effect parameter G. Explicit expressions for the excitation force and mean drift force were derived by Wang and Ren (1994) and Cong and Liu (2020), respectively.

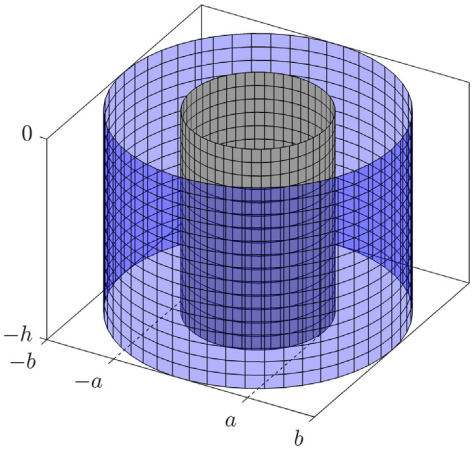

Fig. 2. Mesh used for verification of BEM results against analytical model for wave forces on bottom-fixed vertical cylinder with porous outer wall for the case with outer cylinder radius $b = 2a$ and water depth $h = 3a$. Translucent blue panels are porous, grey panels are non-porous. Mesh has 750 panels on solid inner cylinder and 750 panels on porous outer cylinder. (For interpretation of the references to colour in this figure legend, the reader is referred to the web version of this article.)

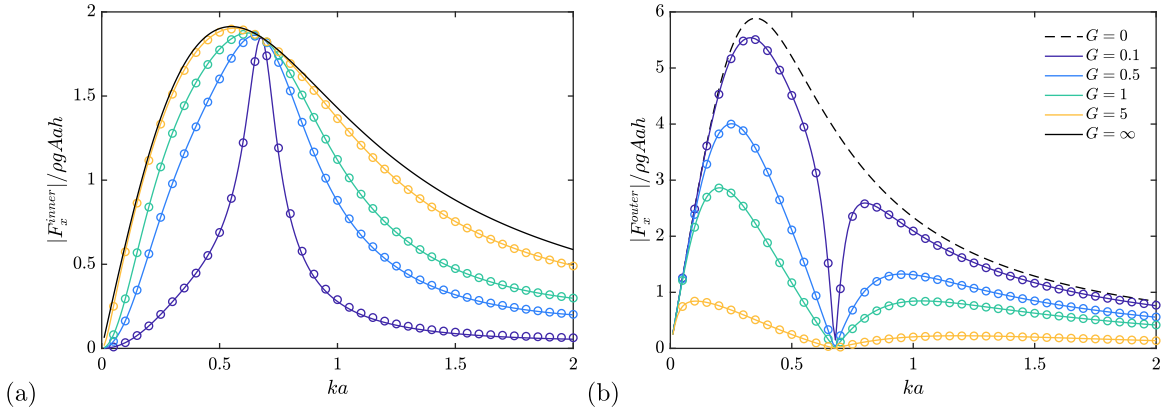

Fig. 3. Comparison of magnitude of non-dimensional horizontal excitation force on concentric porous cylinder with $b = 2a$ and $h = 3a$, from analytical model (solid lines) and BEM model (circles) for various values of ka and G. (a) Force on solid inner cylinder. (b) Force on porous outer cylinder.

The case considered for verification has outer cylinder radius $b = 2a$ and water depth $h = 3a$. In the mesh used for the BEM model, the surfaces of the inner and outer cylinders are divided into 15 panels in the vertical direction and 50 panels around the circumference, giving a total of 1500 panels, as shown in Fig. 2. For the removal of irregular frequencies we have used 80 points on free-surface in the interior of the inner cylinder, consisting of four rings of points at radii of $(0.2, 0.4, 0.6, 0.8)a$, with 20 equally-spaced points in each ring.

A comparison of the magnitude of the non-dimensional horizontal excitation force on the inner and outer cylinders from the analytical and BEM models is shown in Fig. 3 for $ka \in [0, 2]$ and $G = 0.1$, 0.5, 1 and 10. The forces predicted from the two models agree well over the range of conditions considered. There are frequencies for which the force on the outer cylinder goes to zero. For the present case, the first zero occurs at $ka \approx 0.68$. In the vicinity of this frequency, the BEM model replicates the behaviour of the force predicted by the analytical model on both the inner and outer cylinder.

Fig. 4 compares the far-field and porous components of the non-dimensional drift force from the analytical and BEM models. Both the far-field and porous components of the drift force from the BEM model agree well with the analytical calculations for the full range of frequencies and values of G considered.

7. Case study: Truncated cylinder with porous outer wall

In this section we consider the wave-induced forces and motions of a truncated vertical cylinder radius a and draft d, surrounded by a porous outer cylinder of radius b, in infinite water depth. The inner cylinder is assumed to be solid and have a flat solid base. The base section between the inner and outer cylinders is assumed to be porous. Throughout this

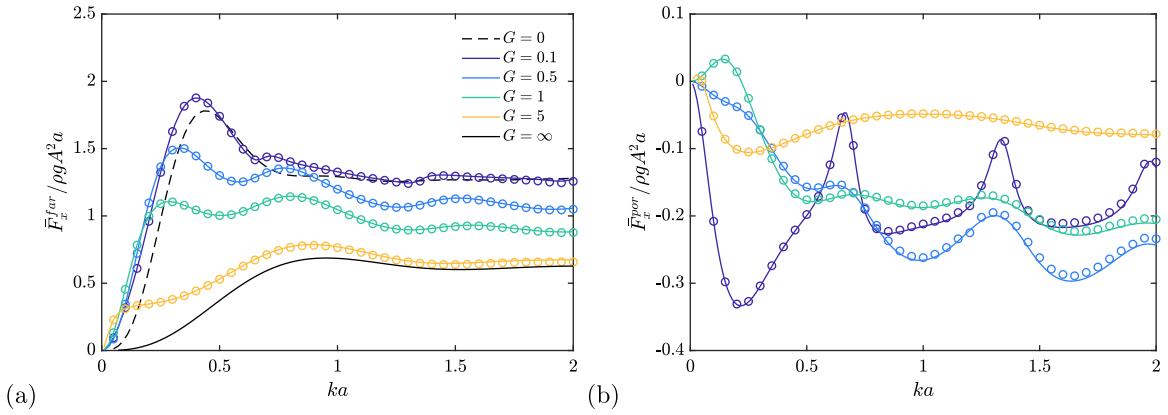

Fig. 4. Comparison of horizontal mean drift force on concentric porous cylinder with $b = 2a$ and $h = 3a$, from analytical model (solid lines) and BEM model (circles) for various values of ka and G. (a) Far-field component. (b) Porous component.

case study we assume a fixed ratio between the draft and radius of the inner cylinder of $d = 4a$ and a fixed ratio between the inner and outer cylinder radius of $b = 2a$. The numerical mesh used in the case studies is shown in Fig. 5 and consists of 1560 panels, with $N_E = 300$, $N_I = 480$ and $N_P = 780$. The pressure drop across the porous surfaces is assumed to be quadratic, with drag coefficient C_f given by (29) with $\mu = 0.5$. The holes in the porous surface are assumed to be closely spaced, so that inertial effects can be neglected and we can set $L = 0$.

From (28) it is evident that a change in the wave amplitude has the same effect on normalised forces and motions as a change in porous drag coefficient C_f. It is therefore reasonable to fix either wave amplitude or steepness and consider only the effect of varying C_f. However, the variation of hydrodynamic coefficients and body motions with wave frequency is different depending on whether wave steepness or amplitude is held constant. Both options lead to non-physical results in either the low-frequency or high-frequency limits. If the steepness is held fixed, then $A \to \infty$ as $k \to 0$, whereas if A is held fixed then $kA \to \infty$ as $k \to \infty$. Mackay and Johanning (2020) considered the asymptotic behaviour of wave forces on a vertical porous wall for long and short waves under the assumptions of both constant amplitude and constant steepness waves. It was shown that the porous wall acts like a solid wall for $k \to 0$ when steepness is held constant or for $k \to \infty$ when amplitude is held constant. In both these cases the horizontal velocity of the incident wave tends to infinity and hence the drag force experienced by the fluid through the porous boundary tends to infinity as well, making the porous boundary behave like a solid boundary.

For the current work we have opted to hold the wave amplitude fixed rather than the steepness, for two reasons. Firstly, in the present case, the effects of the porous outer wall on the motion response are of more interest at lower frequencies, so it makes sense to use physically realistic wave amplitudes at these frequencies. Secondly, it is useful to use a consistent approach for both the radiation and diffraction problems. For the radiation problems it makes less sense to hold $k\xi_j$ fixed, than to hold ξ_j fixed. The wave amplitude has therefore been fixed (arbitrarily) at $A = 0.5a$ for the diffraction problem and motion response problems considered below. This leads to physically unrealistic wave steepness for higher values of ka, but these results are included for illustration. The motion amplitude for the radiation cases is set as $\xi_1 = \xi_3 = 0.5a$ and $\xi_5 = 10°$. Pitch motions and moments are taken about the mean free surface at centre of the inner cylinder.

The results below are presented for various values of the porosity of the outer cylinder, in non-dimensional form. The effects of changing the wave or motion amplitude can be inferred from these results. However, it is important to note that the proportional effect of changing wave or motion amplitude is equivalent to the proportional effect of changing C_f rather than τ, and under Molin's model, $C_f = (1 - \tau)/\mu\tau^2$.

7.1. Excitation forces

The magnitude of the excitation forces and moments in modes 1, 3 and 5 (surge, heave and pitch) are shown in Fig. 6, for the diffraction problem, where the body is held fixed in waves. Results are shown for various values of porosity in the range $\tau = 0.05$ – 0.5, together with the two bounding cases of a solid outer cylinder ($\tau = 0$) and no outer cylinder ($\tau = 1$). The cases $\tau = 0$ and 1 are run using a standard BEM code, which does not account for porosity. The excitation forces shown are the total force on the structure, rather than the force on the inner and outer cylinders shown in the verification case. The excitation forces tend to those for the limiting cases of a solid outer cylinder and no outer cylinder as $\tau \to 0$ and 1, respectively. However, there is a reduction in the surge and pitch forces at $ka \approx 0.68$. This is similar to the verification case of bottom fixed concentric cylinders with linear pressure drop, where a resonance in the fluid motion between the inner and outer cylinders causes the force on the outer cylinder to decrease to zero. The behaviour of the surge force and pitch motion are very similar. For ka above 1, the surge force on the combined structure is slightly

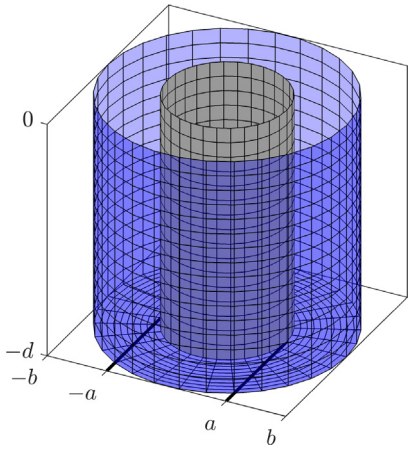

Fig. 5. Example of mesh used for case study of wave forces on truncated vertical cylinder with porous outer wall. The case shown has outer cylinder radius $b = 2a$ and draft $d = 4a$. Translucent blue panels are porous, grey panels are non-porous. (For interpretation of the references to colour in this figure legend, the reader is referred to the web version of this article.)

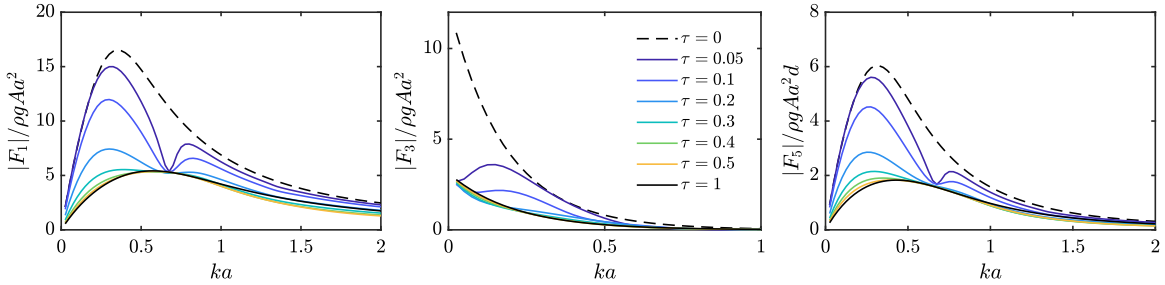

Fig. 6. Normalised magnitude of surge, heave and pitch excitation forces on truncated concentric cylinders with $b = 2a$ and $d = 4a$ and quadratic pressure drop, against ka for various outer cylinder porosity τ.

reduced for $\tau \geq 0.3$, compared to the case with no outer cylinder. However, for lower frequencies there is a significant increase in the surge excitation force for all porosities. The behaviour of the heave excitation force is slightly different, with the porous outer wall causing an increase in the force at higher frequencies and a small reduction in the force at lower frequencies.

7.2. Mean drift force

The horizontal component of the mean drift force is shown in Fig. 7. Panel (a) shows the far-field component and panel (b) shows the porous component. At low frequencies, the far-field component shows an increase relative to the case with a solid outer cylinder. This is somewhat offset by the porous component, which generally acts in the opposite direction to the far-field component. However, at lower frequencies, the total drift force still exhibits an increase relative to the case with a solid outer cylinder. The porous component of the drift force exhibits a similar behaviour to the case of the bottom-fixed cylinders with a linear pressure drop, shown in Fig. 4(b). For the bottom-fixed case, the results of Cong and Liu (2020) indicate that the mean drift force quickly tends to a limit as the water depth increases. So the similar behaviour of the porous component observed here for the truncated cylinder in infinite water depth is understandable.

7.3. Added mass

The added mass (or inertia) for the surge, heave and pitch modes are shown in Fig. 8, together with the values for the cases with a solid outer cylinder and no outer cylinder. For the case with a solid outer cylinder, the mass (or moment of inertia) of the fluid between the inner and outer cylinders has been added to the calculated added mass values. However, the motion of this fluid is not accounted for (i.e. it is assumed to be stationary). The added mass for the porous cases varies between the two bounding cases of no outer cylinder or a solid outer cylinder. However, for the surge mode for the case with a near-solid outer cylinder with $\tau = 0.05$, the resonant sloshing motion of the fluid between the inner and outer cylinders at $ka \approx 0.68$ causes a large increase in the added mass just below this frequency and a large decrease just above this frequency. The effect is decreased as the porosity increases and is less significant in the pitch mode.

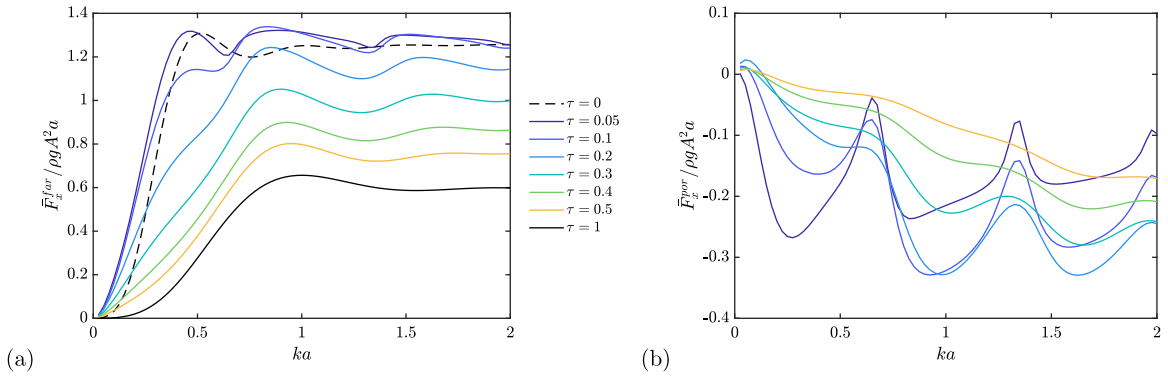

Fig. 7. Normalised horizontal mean drift force on truncated concentric cylinders with $b = 2a$ and $d = 4a$ and quadratic pressure drop, against ka for various outer cylinder porosity τ. (a) Far-field component. (b) Porous component.

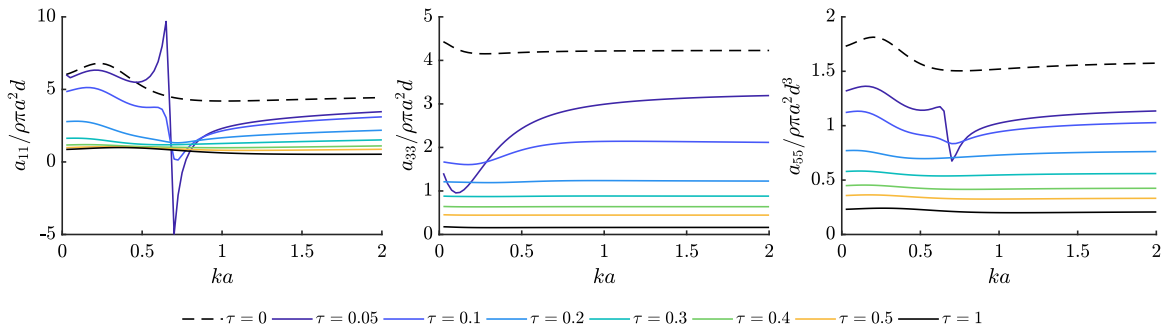

Fig. 8. Normalised added mass (or moment of inertia) in surge, heave and pitch for truncated concentric cylinders with $b = 2a$ and $d = 4a$ and quadratic pressure drop, against ka for various outer cylinder porosity τ.

7.4. Damping

The normalised damping coefficients for the surge, heave and pitch modes are shown in Fig. 9. Note that the colour scale used in this figure differs from previous figures, as a larger range of values of porosity have been used. The three rows of the plots show the total damping, radiation damping and porous damping. For the cases with porous outer cylinders, the total damping is in excess of the case with no outer cylinder for all frequencies shown and significantly in excess of the case with a solid outer cylinder in some cases. In particular, the damping is significantly increased at low and high frequencies, where the radiation damping is low. Looking at the split between the two components of the damping, it is clear that the damping due to dissipation through the porous surface has a larger contribution than wave radiation.

The wave radiation component follows a similar pattern to the excitation forces. Although the standard Haskind relations do no hold for the case of quadratic dissipation, the strong correspondence between the radiation damping and excitation forces indicates that the contribution from the integral over the porous surface in (73) is relatively small. For the surge and pitch modes, the radiation damping is bounded by the limiting case of a solid outer cylinder, but at higher frequencies the damping is lower than in the case with no outer cylinder for some values of porosity. For the heave mode the radiation damping at higher frequencies can exceed that for the case with a solid outer cylinder. This is potentially due to the additional motion of the fluid between the inner and outer cylinder, which may cause an additional contribution to the radiated waves.

There is a sharp decrease in the radiation damping in surge and pitch at $ka \approx 0.68$, where the resonance in the fluid motion between the inner and outer cylinders occurs. At these frequencies, the porous damping in surge and pitch show a sharp increase due to the increased fluid motion.

The normalised porous damping is relatively constant with frequency compared to radiation damping, except for the increase around the resonance at $ka \approx 0.68$. For constant motion amplitude ξ_j, (70) indicates that $b_{jj}^{por}/\rho\omega$ is dependent on the porous drag coefficient C_f and normalised velocity w_n only. As $b_{jj}^{por}/\rho\omega$ is approximately constant with frequency for the cases with higher porosity, this indicates that w_n is approximately constant with frequency also.

As the porosity increases from zero, the porous damping initially increases, then decreases again. Due to the equivalent effect of changes in C_f and ξ_j, this effect can also be interpreted as damping initially increasing with motion amplitude then decreasing after some point. The porosity that results in the maximum damping is dependent on both the mode of

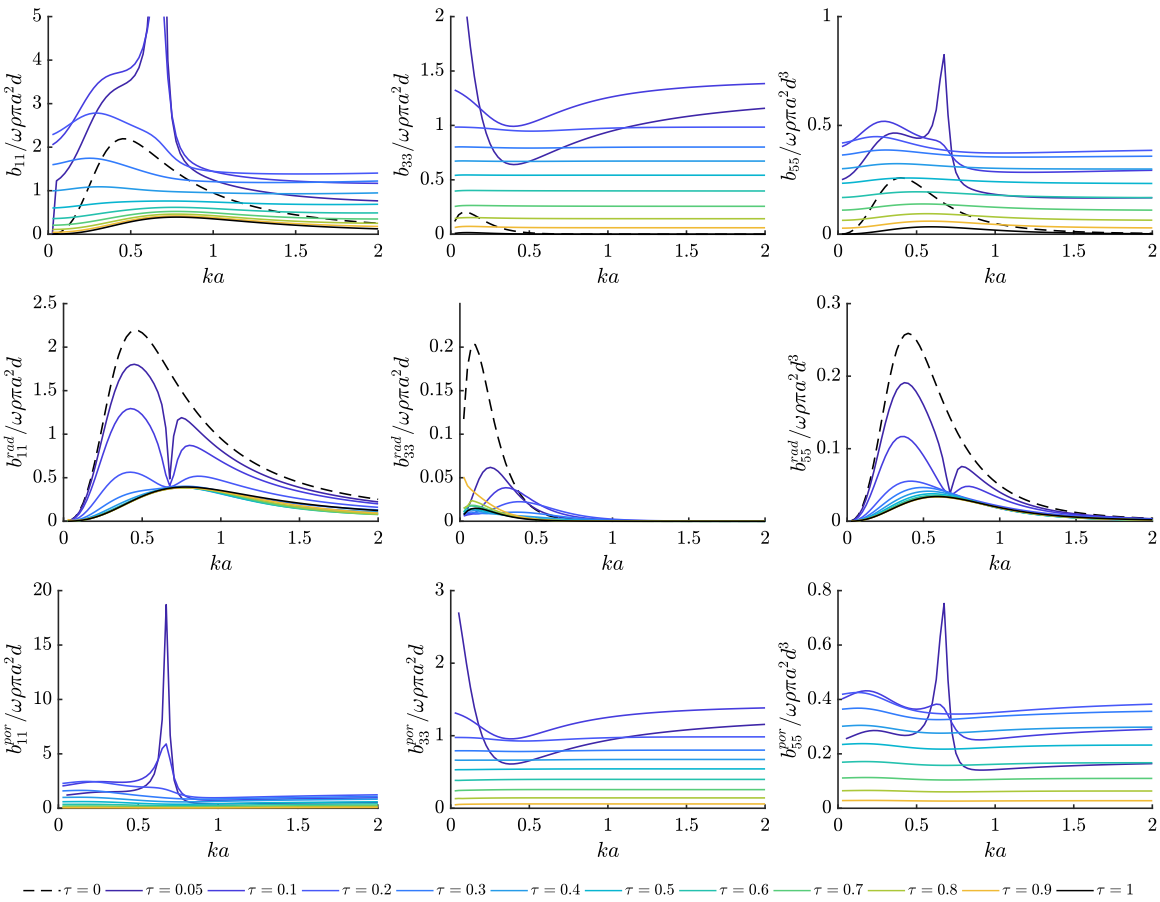

Fig. 9. Normalised damping coefficients in surge, heave and pitch for truncated concentric cylinders with $b = 2a$ and $d = 4a$ and quadratic pressure drop, against ka for various outer cylinder porosity τ. Top row: total damping. Middle row: Radiation damping. Bottom row: Porous damping.

motion and the frequency, and is in the range $\tau = 0.1$–0.2 for the present case. The porous component of the damping decreases more slowly as the porosity increases than the radiation damping. The influence of the porous outer cylinders with $\tau > 0.5$ is negligible for the radiation damping, whereas the porous component of the damping is still significant for $\tau = 0.9$.

7.5. Motion RAOs

In this section we consider the motion response amplitude operator (RAO) for the structure, where the RAO in mode j is defined as $\text{RAO}_j = |\xi_j|/A$. For simplicity, we consider a single degree-of-freedom case, with the cylinder motion constrained to surge only. This could be interpreted as, for example, an approximation to the motion of a tension leg platform (TLP) with a stiff mooring. The mass of the solid inner cylinder is assumed to be equal to the mass of displaced water: $m = \rho\pi a^2 d$. The porous outer cylinder is assumed to be infinitesimally thin and have negligible mass. The cylinder is subject to a mooring restoring force in the surge direction. The stiffness of the mooring in the surge direction is assumed (somewhat arbitrarily) to be equal to the hydrostatic stiffness in heave, so that $C_m = \rho g \pi a^2$, giving a relatively loose restraint in the surge direction and a low frequency resonant response of $ka \approx 0.13$. The mass and damping of the mooring is assumed to be negligible.

To obtain a more realistic response around the resonant frequency for the cases with either no outer cylinder or a solid outer cylinder, we assume that the surge motion is subject to a viscous drag force, given by $F_d(r) = \rho\, r\, d\, C_d\, |U_1|\, U_1$, where $U_1 = \text{Re}\left\{e^{i\omega t} i\omega\xi_1\right\}$ is the surge velocity and $r = a$ for the case with no outer cylinder and $r = b$ when a solid or porous outer cylinder is present. Vortex shedding is expected to be reduced for the porous cylinders. However, in absence of a model for how the drag coefficient is affected by the porosity, we make the simplifying assumption that there is no drag on the porous cylinder and that drag on the solid inner cylinder is unchanged by the addition of the porous outer cylinder. To solve the equation of motion, a linearised drag damping coefficient can be defined using Lorenz's principle

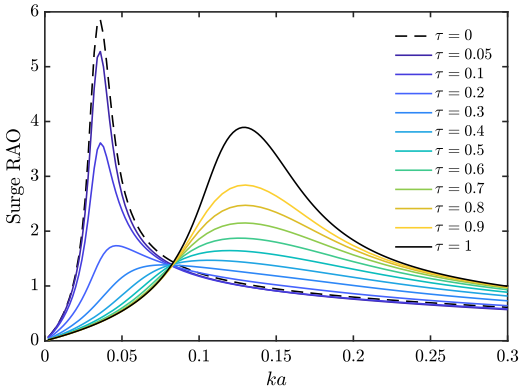

Fig. 10. Surge motion RAO for truncated concentric cylinders with $b = 2a$ and $d = 4a$ and quadratic pressure drop, against ka for various outer cylinder porosity τ.

of equivalent work, as $b_d = \frac{8}{3\pi}\rho\,\omega\,r\,d\,C_d\,|\xi_1|$. The equation of motion for the solid body can then be written

$$F_1 = \left(C_m - \omega^2(m + a_{11}) + i\omega(b_{11} + b_d)\right)\xi_1, \tag{83}$$

which must be solved iteratively due to the dependence of b_d on ξ_1. For the case with porous outer cylinders, the equation of motion becomes

$$F_{H,1} = \left(C_m - m\omega^2 + i\omega b_d\right)\xi_1. \tag{84}$$

For the calculations presented here, a constant drag coefficient of $C_d = 1$ has been used.

From the Haskind relation (74) we see that, for the solid cylinder, the surge radiation damping coefficient tends to zero much faster than the excitation force as $K \to 0$. Similarly, since the linearised drag damping coefficient is proportional to ω, the viscous drag damping also reduces as $K \to 0$. This implies that as the resonant frequency is reduced, the motion RAO in surge will increase. Using the Haskind relation, it can be shown that for an axisymmetric solid body oscillating in the surge direction, the RAO for the resonant frequency tends to $8\rho gA/(k^2|F_j|)$ as $k \to 0$ (neglecting viscous drag forces). This implies that increasing the damping, using porous materials could potentially be beneficial in reducing low frequency resonant motions of floating structures.

The surge RAO for the concentric cylinder structure is shown in Fig. 10, together with the limiting cases of a solid outer cylinder ($\tau = 0$) and no outer cylinder ($\tau = 1$). The mooring stiffness is identical in all cases. The case with the solid outer cylinder has been calculated in the same way as for the case with no outer cylinder, i.e. ignoring the effects of the fluid motion between the inner and outer cylinders. Since the first resonant frequency for the internal fluid is significantly above the frequency range shown, neglecting the internal fluid motion has negligible effect on the results.

For the case with the solid outer cylinder, the mass and added mass is increased, reducing the resonant frequency compared to the case with no outer cylinder. As discussed above, this causes an increase in the peak RAO. As the porosity of the outer cylinder is increased, the added mass is reduced, causing an increase in the resonant frequency. In the radiation only case, the total damping increases initially as the porosity increases, then decreases again. Although it is not possible to separate the excitation and radiation forces in this case, a similar effect can be seen in the motion response. The configuration with an outer cylinder porosity of $\tau = 0.3$ has the lowest peak RAO across all frequencies. The configurations with higher porosities have lower response at low frequencies, as these configurations behave more like the case with no outer cylinder. At higher frequencies, the configurations with lower porosities have lower response, since these behave more like the case with a solid outer cylinder. In general, we can conclude that adding a porous outer cylinder has two effects on the motion response: a shift of the resonant response to lower frequencies due to increased added mass, and a reduction in the peak response due to increased damping.

8. Conclusions

A BEM model has been presented for calculating wave forces and motions of structures composed of solid and porous surfaces, with either a linear or quadratic pressure–velocity relation on the porous surface. In the case of the quadratic pressure–velocity relations, the model solves for the combined motion response and wave forces on structure simultaneously. Solutions for the radiation and diffraction problems are obtained as special cases of the general solution for body motions in waves.

The method has been verified against an analytical solution for a bottom-fixed vertical cylinder with a porous outer cylinder, subject to a linear pressure–velocity relation. It was shown that the excitation forces and far-field component of the drift force agree well between the analytical solution and BEM calculations. The method used for removing the

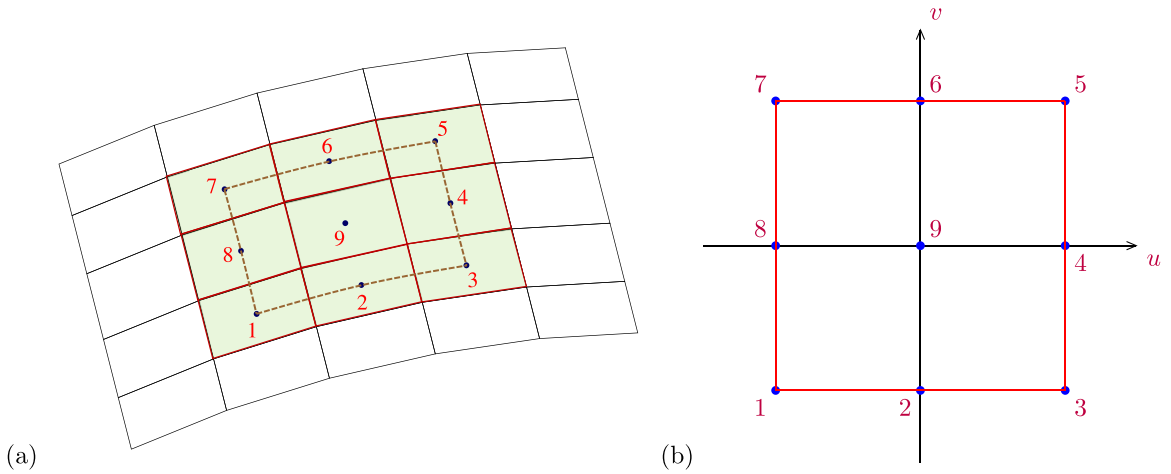

Fig. 11. The 9-point quadrilateral patch in physical space (a) and parametric space (b).

effects of irregular frequencies was successful for suppressing these effects in the potential, first-order wave forces and mean drift force.

Wave forces on a floating truncated cylinder with a porous outer cylinder were considered for the case of a quadratic pressure drop across the porous cylinder. The effect of the porous outer cylinder is, in general, to increase the excitation force and added mass relative to the case with no outer cylinder. However, the damping due to dissipation of energy through the porous surface is significantly increased, especially at low and high frequencies where the radiation damping is low. The effect of the porous outer cylinder on the motion response is to reduce the resonant frequency due to the increased added mass and to reduce the amplitude of the motion response due to the increased damping. This could potentially be beneficial for motion damping of floating structures subject to low frequency resonant responses.

CRediT authorship contribution statement

Ed Mackay: Conceptualization, Methodology, Software, Formal analysis, Writing - original draft. **Hui Liang:** Methodology, Software, Writing - review & editing. **Lars Johanning:** Funding acquisition, Supervision.

Declaration of competing interest

The authors declare that they have no known competing financial interests or personal relationships that could have appeared to influence the work reported in this paper.

Acknowledgement

This work was funded under EPSRC, United Kingdom grant EP/R007519/1.

Appendix. Calculation of fluid velocities on the body surface using quadratic interpolation

The fluid velocity tangential to each panel can be calculated using quadratic interpolation of the potentials on adjacent panels. For each panel, we construct a patch with $3 \times 3 = 9$ panels, as shown in Fig. 11(a). A unique quadratic surface can be defined which takes values ψ_j, $j = 1, \ldots, 9$, at points 1–9, where ψ could represent any physical quantity, such as the velocity potential, its derivatives, geometrical coordinates in physical space, etc. To define the quadratic surface, we define a local coordinate system (u, v) over the patch, where $-1 \leq u \leq 1$ and $-1 \leq v \leq 1$ and $(u, v) = (-1, -1)$ at point 1 and $(u, v) = (1, 1)$ at point 5 (see Fig. 11(b)). The quadratic surface can then be written in the (u, v) coordinates as the weighted sum of the values at points 1–9:

$$\psi(u, v) = \sum_{j=1}^{9} \mathcal{N}_j(u, v)\psi_j, \tag{A.1}$$

where $\mathcal{N}_j(u, v)$ are quadratic shape functions defined by

$$\begin{aligned}
\mathcal{N}_1(u, v) &= +(u-u^2)(v-v^2)/4,\\
\mathcal{N}_2(u, v) &= -(1-u^2)(v-v^2)/2,\\
\mathcal{N}_3(u, v) &= -(u+u^2)(v-v^2)/4,\\
\mathcal{N}_4(u, v) &= +(u+u^2)(1-v^2)/2,\\
\mathcal{N}_5(u, v) &= +(u+u^2)(v+v^2)/4,\\
\mathcal{N}_6(u, v) &= +(1-u^2)(v+v^2)/2,\\
\mathcal{N}_7(u, v) &= -(u-u^2)(v+v^2)/4,\\
\mathcal{N}_8(u, v) &= -(u-u^2)(1-v^2)/2,\\
\mathcal{N}_9(u, v) &= +(u^2-1)(v^2-1).
\end{aligned} \tag{A.2}$$

Using the chain-rule, the spatial derivatives of potential ϕ can be written as

$$\begin{bmatrix} \phi_u \\ \phi_v \\ \phi_n \end{bmatrix} = \begin{bmatrix} x_u & y_u & z_u \\ x_v & y_v & z_v \\ n_x & n_y & n_z \end{bmatrix} \begin{bmatrix} \phi_x \\ \phi_y \\ \phi_z \end{bmatrix} \quad \Longrightarrow \quad \begin{bmatrix} \phi_x \\ \phi_y \\ \phi_z \end{bmatrix} = \begin{bmatrix} x_u & y_u & z_u \\ x_v & y_v & z_v \\ n_x & n_y & n_z \end{bmatrix}^{-1} \begin{bmatrix} \phi_u \\ \phi_v \\ \phi_n \end{bmatrix}, \tag{A.3}$$

where the subscript denotes partial differentiation. The normal derivative ϕ_n is known from the body boundary condition and the partial derivatives with respect to u and v can be obtained by directly differentiating the shape functions

$$\begin{Bmatrix} x_u \\ y_u \\ z_u \\ \phi_u \end{Bmatrix} = \sum_{j=1}^{9} \frac{\partial \mathcal{N}_j(u, v)}{\partial u} \begin{Bmatrix} x_j \\ y_j \\ z_j \\ \phi_j \end{Bmatrix} \quad \text{and} \quad \begin{Bmatrix} x_v \\ y_v \\ z_v \\ \phi_v \end{Bmatrix} = \sum_{j=1}^{9} \frac{\partial \mathcal{N}_j(u, v)}{\partial v} \begin{Bmatrix} x_j \\ y_j \\ z_j \\ \phi_j \end{Bmatrix}. \tag{A.4}$$

where possible, the fluid velocity on a panel is calculated by centring the patch at the panel. For panels on the edge of the mesh, the same approach can still be used to derive the derivative of the potential on any panel of the patch.

References

Chen, X., 1993. Evaluation de la fonction de Green du probleme de diffraction/radiation en profondeur d'eau finie-une nouvelle methode rapide et precise. In: Actes des 4e Journees de l'Hydrodynamique. Nantes, France. pp. 371–384.

Chen, K.H., Chen, J.T., Lin, S.Y., Lee, Y.T., 2004. Dual boundary element analysis of normal incident wave passing a thin submerged breakwater with rigid, absorbing, and permeable boundaries. J. Waterway Port Coast. Ocean Eng. 130 (4), 179–190. http://dx.doi.org/10.1061/(ASCE)0733-950X(2004)130:4(179).

Chen, B., Wang, L., Ning, D., Johanning, L., 2019. CFD analysis on wave load mitigation effect of a perforated wall on offshore structure. In: Proceedings of the Twenty-ninth (2019) International Ocean and Polar Engineering Conference, Honolulu, Hawaii, USA, June 16–21, 2019. pp. 3653–3658.

Cho, I.H., Kim, M.H., 2008. Wave absorbing system using inclined perforated plates. J. Fluid Mech. 608, 1–20. http://dx.doi.org/10.1017/S0022112008001845.

Chwang, A.T., 1983. A porous wavemaker theory. J. Fluid Mech. 132, 395–406.

Chwang, A.T., Li, W., 1983. A piston-type porous wavemaker theory. J. Eng. Math. 17 (4), 301–313. http://dx.doi.org/10.1007/BF00040174.

Cong, P., Liu, Y., 2020. Local enhancements of the mean driftwave force on a vertical column shielded by an exterior thin porous shell. J. Mar. Sci. Eng. 8 (5), 1–14. http://dx.doi.org/10.3390/JMSE8050349.

Crowley, S., Porter, R., 2012. An analysis of screen arrangements for a tuned liquid damper. J. Fluids Struct. 34, 291–309. http://dx.doi.org/10.1016/j.jfluidstructs.2012.06.001.

Dai, J., Wang, C.M., Utsunomiya, T., Duan, W., 2018. Review of recent research and developments on floating breakwaters. Ocean Eng. 158, 132–151.

Dokken, J., Grue, J., Karstensen, L.P., 2017a. Wave analysis of porous geometry with linear resistance law. J. Mar. Sci. Appl. 16 (4), 480–489. http://dx.doi.org/10.1007/s11804-017-1438-2.

Dokken, J.S., Grue, J., Karstensen, L.P., 2017b. Wave forces on porous geometries with linear and quadratic pressure-velocity relations. In: 32nd International Workshop on Water Waves and Floating Bodies. Dalian, China.

Faltinsen, O.M., Firoozkoohi, R., Timokha, A.N., 2011. Steady-state liquid sloshing in a rectangular tank with a slat-type screen in the middle: Quasilinear modal analysis and experiments. Phys. Fluids 23 (4), http://dx.doi.org/10.1063/1.3562310.

Feng, X., Chen, X.B., Dias, F., 2018. A potential flow model with viscous dissipation based on a modified boundary element method. Eng. Anal. Bound. Elem. 97 (February), 1–15. http://dx.doi.org/10.1016/j.enganabound.2018.09.004.

Gayen, R., Mondal, A., 2014. A hypersingular integral equation approach to the porous plate problem. Appl. Ocean Res. 46, 70–78. http://dx.doi.org/10.1016/j.apor.2014.01.006.

Huang, Z., Li, Y., Liu, Y., 2011. Hydraulic performance and wave loadings of perforated / slotted coastal structures: A review. Ocean Eng. 38 (10), 1031–1053.

Ijima, T., Chou, C.R., Yoshida, A., 1976. Method of analyses for two-dimensional water wave problems. In: Fifteenth Coastal Engineering Conference. Hawaii, USA, pp. 2717–2736. http://dx.doi.org/10.9753/icce.v15.155.

Isaacson, M., Premasiro, S., Yang, G., 1998. Wave interaction with vertical slotted barrier. J. Waterway Port Coast. Ocean Eng. 124, 118–126.

John, F., 1950. On the motion of floating bodies II. Simple Harmonic Motion. Comm. Pure Appl. Math. 3, 45–101. http://dx.doi.org/10.1002/cpa.3160030106.

Lau, S.M., Hearn, G.E., 1989. Suppression of irregular frequency effects in fluid–structure interaction problems using a combined boundary integral equation method. Internat. J. Numer. Methods Fluids 9 (7), 763–782. http://dx.doi.org/10.1002/fld.1650090703.

Lee, C.P., Ker, W.K., 2002. Coupling of linear waves and a hybrid porous TLP. Ocean Eng. 29, 1049–1066.

Lee, C.-H., Newman, J., 2005. Computation of wave efects using the panel method. In: Numerical Models in Fluid-Structure Interaction, Vol. 18. pp. 211–251. http://dx.doi.org/10.2495/978-1-85312-837-0/06.
Lee, C., Zhu, X., 2018. Application of hyper-singular integral equations for a simplified model of viscous dissipation. In: 28th International Ocean and Polar Engineering Conference. Sapporo, Japan. pp. 345–350.
Li, Y., Liu, Y., Teng, B., 2006. Porous effect parameter of thin permeable plates. Coast. Eng. J. 48 (4), 309–336. http://dx.doi.org/10.1142/S0578563406001441.
Liang, H., Ouled Housseine, C., Chen, X., Shao, Y., 2020. Efficient methods free of irregular frequencies in wave and solid / porous structure interactions. J. Fluids Struct. 98, 103130. http://dx.doi.org/10.1016/j.jfluidstructs.2020.103130.
Linton, C., Mciver, P., 2001. Mathematical Techniques for Wave / Structure Interactions. Chapman & Hall/CRC.
Liu, Y., Li, Y.C., 2016. Predictive formulas in terms of Keulegan–Carpenter numbers for the resistance coefficients of perforated walls in Jarlan-type caissons. Ocean Eng. 114, 101–114. http://dx.doi.org/10.1016/j.oceaneng.2016.01.007.
Liu, Y., Li, H.J., 2017. Iterative multi-domain BEM solution for water wave reflection by perforated caisson breakwaters. Eng. Anal. Bound. Elem. 77 (238), 70–80. http://dx.doi.org/10.1016/j.enganabound.2016.12.011.
Liu, Y., Li, H.J., Li, Y.C., 2012. A new analytical solution for wave scattering by a submerged horizontal porous plate with finite thickness. Ocean Eng. 42, 83–92. http://dx.doi.org/10.1016/j.oceaneng.2012.01.001.
Mackay, E., 2019. Consistent expressions for the free-surface Green function in finite water depth. Appl. Ocean Res. 93 (May), 101965. http://dx.doi.org/10.1016/j.apor.2019.101965.
Mackay, E., Feichtner, A., Smith, R.E., Thies, P.R., Johanning, L., 2018. Verification of a boundary element model for wave forces on structures with porous elements. In: 3rd International Conference on Renewable Energies Offshore, RENEW 2018. pp. 341–350.
Mackay, E., Johanning, L., 2020. Comparison of analytical and numerical solutions for wave interaction with a vertical porous barrier. Ocean Eng. 199 (February), 107032. http://dx.doi.org/10.1016/j.oceaneng.2020.107032.
Mackay, E., Johanning, L., Ning, D., Qiao, D., 2019. Numerical and experimental modelling of wave loads on thin porous sheets. In: 38th International Conference on Ocean, Offshore and Arctic Engineering. pp. 1–10.
Mackay, E., Shi, W., Qiao, D., Gabl, R., Davey, T., Ning, D., Johanning, L., 2020. Numerical and experimental modelling of wave interaction with fixed and floating porous cylinders. Preprint availabe from http://dx.doi.org/10.13140/RG.2.2.16339.20002 (submitted for publication).
Mallayachari, V., Sundar, V., 1994. Reflection characteristics of permeable seawalls. Coast. Eng. 23 (1–2), 135–150. http://dx.doi.org/10.1016/0378-3839(94)90019-1.
Maruo, H., 1960. The drift of a body floating in waves. J. Ship Res. 4 (3), 1–10.
Mei, C.C., 1983. The Applied Dynamics of Ocean Surface Waves. World Scientific, p. 768.
Mentzoni, F., Kristiansen, T., 2019. Numerical modeling of perforated plates in oscillating flow. Appl. Ocean Res. 84, 1–11.
Molin, B., 2011. Hydrodynamic modeling of perforated structures. Appl. Ocean Res. 33 (1), 1–11.
Molin, B., Fourest, J.-M., 1992. Numerical modeling of progressive wave absorbers. In: 7th International Workshop Water Waves & Floating Bodies.
Molin, B., Remy, F., 2013. Experimental and numerical study of the sloshing motion in a rectangular tank with a perforated screen. J. Fluids Struct. 43, 463–480. http://dx.doi.org/10.1016/j.jfluidstructs.2013.10.001.
Molin, B., Remy, F., 2015. Inertia effects in TLD sloshing with perforated screens. J. Fluids Struct. 59, 165–177. http://dx.doi.org/10.1016/j.jfluidstructs.2015.09.004.
Moré, J., 1978. The Levenberg–Marquardt algorithm: Implementation and theory. In: Watson, G. (Ed.), Numerical Analysis. In: Lecture Notes in Mathematics, vol. 630, Springer, Berlin, pp. 105–116.
Newman, J., 1967. The drift force and moment on ships in waves. J. Ship Res. 11 (1), 51–60.
Newman, J., 1976. The interaction of stationary vessel with regular waves. In: 11th Symposium on Naval Hydrodynamics. pp. 491–501.
Newman, J.N., 1986. Distributions of sources and normal dipoles over a quadrilateral panel. J. Eng. Math. 20 (2), 113–126. http://dx.doi.org/10.1007/BF00042771.
Ning, D.Z., Zhao, X.L., Teng, B., Johanning, L., 2017. Wave diffraction from a truncated cylinder with an upper porous sidewall and an inner column. Ocean Eng. 130 (July 2016), 471–481. http://dx.doi.org/10.1016/j.oceaneng.2016.11.043.
Ouled Housseine, C., de Hauteclocque, G., Malencia, S., Chen, X.-b., 2018. Hydrodynamic interactions of the truncated porous vertical circular cylinder with water waves. In: 37th International Conference on Ocean, Offshore and Arctic Engineering. Madrid, Spain. OMAE2018-78221.
Poguluri, S.K., Cho, I.H., 2020. Analytical and numerical study of wave interaction with a vertical slotted barrier. Ships Offshore Struct. 1–13. http://dx.doi.org/10.1080/17445302.2020.1790299.
Sahoo, T., Lee, M., Chwang, A.T., 2000. Trapping and generation of waves by vertical porous structures. J. Eng. Mech. 126 (10), 1074–1082.
Sollitt, C., Cross, R., 1972. Wave transformation through permeable breakwaters. In: 13th International Conference on Coastal Engineering. pp. 1827–1846.
Suh, K.D., Kim, Y.W., Ji, C.H., 2011. An empirical formula for friction coefficient of a perforated wall with vertical slits. Coast. Eng. 58 (1), 85–93. http://dx.doi.org/10.1016/j.coastaleng.2010.08.006.
Sulisz, W., 1985. Wave reflection and transmission at permeable breakwaters of arbitrary cross-section. Coast. Eng. 9 (4), 371–386. http://dx.doi.org/10.1016/0378-3839(85)90018-3.
Tait, M.J., El Damatty, A.A., Isyumov, N., Siddique, M.R., 2005. Numerical flow models to simulate tuned liquid dampers (TLD) with slat screens. J. Fluids Struct. 20 (8), 1007–1023. http://dx.doi.org/10.1016/j.jfluidstructs.2005.04.004.
Twu, S.W., Lin, D.T., 1991. On a highly effective wave absorber. Coast. Eng. 15 (4), 389–405. http://dx.doi.org/10.1016/0378-3839(91)90018-C.
Valizadeh, A., Rafiee, A., Francis, V., Rudman, M., Ramakrishnan, B., 2018. An analysis of perforated plate breakwaters. In: Proceedings of the International Offshore and Polar Engineering Conference, Vol. 2018-June. pp. 1174–1180.
Vijay, K.G., Neelamani, S., Sahoo, T., 2019. Wave interaction with multiple slotted barriers inside harbour: Physical and numerical modelling. Ocean Eng. 193 (September), 106623. http://dx.doi.org/10.1016/j.oceaneng.2019.106623.
Vijay, K.G., Nishad, C.S., Neelamani, S., Sahoo, T., 2020. Gravity wave interaction with a wave attenuating system. Appl. Ocean Res. 101 (May), 102206. http://dx.doi.org/10.1016/j.apor.2020.102206.
Vijay, K.G., Sahoo, T., 2018. Retrofitting of floating bridges with perforated outer cover for mitigating wave-induced responses. In: 37th International Conference on Ocean, Offshore and Arctic Engineering. http://dx.doi.org/10.1115/omae2018-77054, OMAE2018-77054.
Wang, K., Ren, X., 1994. Wave interaction with a concentric porous cylinder system. Ocean Eng. 21 (4), 343–360.
Williams, A.N., Li, W., Wang, K.H., 2000. Water wave interaction with a floating porous cylinder. Ocean Eng. 27, 1–28.
Yu, X., 1995. Diffraction of water waves by porous breakwaters. J. Waterway Port Coast. Ocean Eng. 121 (6), 275–282.
Yueh, C.Y., Chuang, S.H., Wen, C.C., 2016. Wave scattering by submerged composite wavy plate breakwaters using a dual BEM. Ocean Eng. 124, 192–203. http://dx.doi.org/10.1016/j.oceaneng.2016.07.019.
Yueh, C.-y., Tsaur, D.-h., 1999. Wave scattering by submerged vertical plate-type breakwater using composite bem. Coast. Eng. J. 41 (1), 65–83. http://dx.doi.org/10.1142/S057856349900005X.
Zhao, F., Bao, W., Kinoshita, T., Itakura, H., 2010a. Theoretical and experimental study on a porous cylinder floating in waves. J. Offshore Mech. Arct. Eng. 133 (1), 011301. http://dx.doi.org/10.1115/1.4001435.

Zhao, F., Bao, W., Kinoshita, T., Itakura, H., 2010b. Interaction of waves and a porous cylinder with an inner horizontal porous plate. Appl. Ocean Res. 32 (2), 252–259. http://dx.doi.org/10.1016/j.apor.2009.11.003.
Zhao, F., Kinoshita, T., Bao, W., Wan, R., Liang, Z., Huang, L., 2011. Hydrodynamics identities and wave-drift force of a porous body. Appl. Ocean Res. 33 (3), 169–177. http://dx.doi.org/10.1016/j.apor.2011.04.001.